

⁴⁰Ar/³⁹Ar ages in deformed potassium feldspar: Evidence for a microstructural control on Ar isotope systematics

Steven M. Reddy¹ · Graham J. Potts² · Simon P. Kelley³

¹ *Tectonics Special Research Centre, School of Applied Geology, Curtin University of Technology, PO Box U1987, Perth, WA 6845, Australia.*

² *Department of Earth Sciences, The University of Liverpool, Jane Herdman Laboratories, 4 Brownlow Street, Liverpool, L69 3GP, UK.*

³ *Department of Earth Sciences, The Open University, Milton Keynes, MK7 6AA, UK.*

Short Title: ⁴⁰Ar/³⁹Ar ages in deformed K-feldspar

Key Words: geochronology, deformation, microstructure, orientation contrast imaging, diffusion, ultra-violet laser microprobe (UVLAMP), Torridonian, Skye

Correspondence to Steve Reddy (e-mail: S.Reddy@curtin.edu.au)

ABSTRACT

Detailed field and microstructural studies have been combined with high spatial resolution ultra-violet laser $^{40}\text{Ar}/^{39}\text{Ar}$ dating of naturally deformed K-feldspar to investigate the direct relationship between deformation-related microstructure and Ar isotope systematics. The sample studied is a *c.* 1000 Ma Torridonian arkose from Skye, Scotland, that contains detrital feldspars previously metamorphosed at amphibolite-facies conditions *c.* 1700 Ma. The sample was subsequently deformed *c.* 430 Ma ago during Caledonian orogenesis. The form and distribution of deformation-induced microstructures within three different feldspar clasts has been mapped using atomic number contrast and orientation contrast imaging, at a range of scales, to identify intragrain variations in composition and lattice orientation. These variations have been related to thin section and regional structural data to provide a well-constrained deformation history for the feldspar clasts.

143 *in situ* $^{40}\text{Ar}/^{39}\text{Ar}$ analyses measured using ultraviolet laser ablation record a range of apparent ages (317 - 1030 Ma). The K-feldspar showing the least strain records the greatest range of apparent ages from 420 to 1030 Ma, with the oldest apparent ages being found close to the centre of the feldspar away from fractures and the detrital grain boundary. The most deformed K-feldspar yields the youngest apparent ages (317 - 453 Ma) but there is no spatial relationship between apparent age and the detrital grain boundary. Within this feldspar, the oldest apparent ages are recorded from orientation domain boundaries and fracture surfaces where an excess or trapped ^{40}Ar component resides. Orientation contrast images at a similar scale to the Ar analyses illustrate a significant deformation-related microstructural difference between the feldspars and we conclude that deformation plays a significant role in controlling Ar systematics of feldspars at both the inter- and intragrain scales even at relatively low 'bulk' strains. The data show that Ar loss and trapping within the deformed K-feldspars reflects the presence of a deformation-induced population of small diffusion domains in combination with 'short-circuit' diffusion along deformation-induced defects. The complex history of microstructures induced in the K-feldspars during their cooling, alteration, erosion, and sedimentation do not appear to be as significant as deformation-induced microstructures in controlling the distribution of apparent ages at the grain scale.

INTRODUCTION

The $^{40}\text{Ar}/^{39}\text{Ar}$ dating technique is widely applied to potassium-bearing minerals to constrain the thermal history of rocks between temperatures of *c.* 150-500°C. Fundamental to the correct thermochronological interpretation of $^{40}\text{Ar}/^{39}\text{Ar}$ data is an understanding of the processes that influence Ar migration in minerals. However, there is currently considerable debate regarding the ways in which Ar data may be interpreted. Central to this debate is the relative importance of volume diffusion of Ar through the mineral lattice and multipath diffusion of Ar along intracrystalline mineral defects.

Traditionally Ar diffusion in minerals has been considered to be a volume diffusion process. Over 25 years ago, Dodson (1973) outlined a simple "closure temperature" model that assumed volume diffusion and recognised the temperature, grain size and cooling rate controls on isotope migration. In a more complex model, Dodson (1986) illustrated that over geological time scales, volume diffusion should lead to the development of 'closure profiles' displaying a range of ages within individual mineral grains. Recently, more sophisticated volume diffusion models, involving multiple diffusion domains (MDD), have been proposed specifically to interpret Ar data obtained from alkali feldspar (Lovera et al. 1989; Harrison et al. 1991; Lovera et al. 1997). This approach has been applied to a range of geological problems (Quidelleur et al. 1997; Dunlap et al. 1998; Dalrymple et al. 1999; Mock et al. 1999). However, the interpretations are sometimes complex (Mock et al. 1999) and not all samples yield interpretable results (Heizler and Harrison 1991).

Recent detailed electron microscope investigations of undeformed alkali feldspars have demonstrated that alkali feldspars undergo a series of complex microstructural modifications due to subsolvus exsolution, deuteric alteration and chemical reaction over a range of

temperature conditions (Lee et al. 1995; Lee and Parsons 1998). These processes can result in the development of dislocations within the feldspar leading to semi-coherent perthite lamellar interfaces. Deuteric alteration can lead to replacement of regular perthites by incoherent subgrain mosaics (Lee et al. 1995; Lee and Parsons 1997). Such structures may have a significant effect on intragrain diffusion (Harrison 1961; Lai and Morrison 1970; Aifantis 1979; Le Claire and Rabinovitch 1984; Lee and Aldama 1992; Lee 1995; Parsons et al. 1999). Where they form at low temperature, these structures are inconsistent with the assumptions required by MDD theory (Lovera et al. 1997) suggesting that thermal histories derived by this technique may be fundamentally flawed (Villa 1994, Parsons et al. 1999). In addition, recent research has shown that low temperature deformation and grain size reduction transforms argon diffusion characteristics in K-feldspar (Arnaud and Eide 2000).

Given the complexity and controversial nature of the interpretation of Ar data from minerals with relatively simple geological histories, it is not surprising that detailed studies of the effects of deformation on Ar isotope systematics are rare. Theoretical modelling of the effects of deformation-induced grain size changes, the effects of different grain-scale deformation mechanisms and the difference between the temperatures of deformation and isotopic closure illustrate significant complexity even in simple, volume diffusion systems (Reddy and Potts 1999). These complexities will be compounded in natural deforming systems by the development of microfractures, dislocations and subgrain boundaries that will behave as heterogeneously distributed, fast-diffusion pathways (Lee 1995; Villa 1998). However, despite the potential problems, understanding the isotopic evolution of deformed minerals is essential if the timing, duration and rates of deformation are to be better constrained.

Recently, a combination of microstructural imaging techniques with high-spatial resolution, intragrain Ar analyses has been used to investigate Ar isotope distributions in naturally

deformed samples. Integration of laser ablation $^{40}\text{Ar}/^{39}\text{Ar}$ dating with standard petrological work and atomic number contrast (ANC) imaging has been used qualitatively to demonstrate a relationship between deformation and isotopic distribution in structurally well-characterised metamorphic rocks (Reddy et al. 1996; Reddy et al. 1997). $^{40}\text{Ar}/^{39}\text{Ar}$ studies in combination with transmission electron microscopy (TEM) have also provided useful constraints on the relationship between isotope systematics and microstructure (Burgess et al. 1992). However, both of these approaches have limitations.

ANC imaging identifies compositional variations but does not readily identify the sites of intracrystalline deformation that must be established if a direct link between microstructure and argon isotope distribution is to be made. Etching of the sample can reveal feldspar microstructures (Waldron et al. 1994) but the effect of etching on $^{40}\text{Ar}/^{39}\text{Ar}$ ages using surface analysis methods is unknown. TEM analysis is a destructive imaging technique that precludes subsequent $^{40}\text{Ar}/^{39}\text{Ar}$ analysis of the imaged part of the grain. Consequently, imaging of etched samples and TEM studies both require subsequent $^{40}\text{Ar}/^{39}\text{Ar}$ analyses to be undertaken on different parts of the sample. In addition, while TEM is the only technique that allows the actual size of relevant microstructures to be measured, the scale of TEM observations and the scale at which Ar analyses can be made are significantly different. As a result it is difficult to reconcile the two strands of data.

Advancing the study of the relationships between deformation and isotope systematics requires the integration of a high spatial resolution dating technique capable of intragrain analyses with a non-destructive imaging technique that permits recognition of intragrain microstructures at the same scale as the isotope analyses. The recent development and application of orientation contrast (OC) imaging to geological materials, through foreshadowing scanning electron microscopy, provides a non-destructive means of imaging intragrain

microstructure at the μm scale and, through electron backscatter diffraction, quantitative estimates of intragrain deformation (Prior et al. 1996; Prior et al. 1999). These techniques can identify angular misorientations ($< 1^\circ$) within a mineral with the same spatial resolution as Ar laser microprobe analyses, thereby allowing both of the data sets to be obtained from the *same* sites.

In a recent paper, Reddy et al. (1999) outlined the combination of OC imaging with ultra-violet laser microprobe (UVLAMP) $^{40}\text{Ar}/^{39}\text{Ar}$ dating. This first account of combining OC and UVLAMP techniques demonstrated a correlation between intragrain microstructure and preserved $^{40}\text{Ar}/^{39}\text{Ar}$ ages within a single K-feldspar. However, the conclusions that could be drawn were limited because the study did not include feldspars deformed to different degrees by different mechanisms. In this paper, we address these limitations by presenting further analyses from the same sample used by Reddy et al. (1999) to assess the effects of deformation on isotope systematics at both the intra- and intergrain scale. The aim is to develop a clearer understanding of the ways in which deformation may affect isotope systematics in naturally deformed samples so that better techniques and approaches to temporally constrain rock deformation may be established. The new results presented in this study show a strong correlation between deformation intensity and apparent age and confirm that deformation-related microstructures are of fundamental importance in controlling Ar isotope systematics even in rocks deformed at low strains.

Critical to our study is the ability to relate regional structural geology to deformation at the grain scale. Therefore, we present a detailed account of the regional geology and deformation history of the studied sample in a supplementary text (eText1). Within the main body of the paper we present a summary of these data and also provide detailed descriptions of the microstructural characterisation of the different feldspars and the UVLAMP $^{40}\text{Ar}/^{39}\text{Ar}$ data

from the same feldspars. These data are finally integrated and discussed in terms of their significance to the Ar systematics of deformed minerals.

SAMPLING CRITERIA

To maximise the possibility of identifying the effects of deformation microstructures on Ar isotope systematics several criteria were recognised as being essential to successful sample selection. 1) A significant age difference should exist between crystallisation and deformation to maximise the temporal resolution of the isotope measurements. 2) The deformation should be relatively old so that measurable quantities of Ar are available. 3) The sample should have undergone relatively low 'bulk' strain and the deformation should be heterogeneous at the grain scale to facilitate correlations between deformation intensity and apparent age. 4) Deformation should have taken place close to, or preferably below, the closure temperature of the deforming minerals to reduce the effects of the post-deformational thermal history. 5) Distinguishing between those microstructures formed as a result of the deformation and those inherited from initial crystallisation and any earlier deformations must be possible.

To best achieve criteria 4) and 5), we selected a sedimentary sample so that the detrital clast shapes of the feldspar could be used as a marker for pre-and post- depositional microstructural development. By selecting a sedimentary sample we could also ensure that the feldspars we analysed had cooled below their closure temperature since primary crystallisation. This would have been difficult to prove if we had selected a deformed igneous rock. The disadvantage of such a selection is that the alkali feldspars we analysed are likely to have undergone a complex history involving multiple phases of deuteric alteration and diagenesis.

The criteria outlined above were met by a sample of Sleat Group (Stewart 1982) Torridonian sandstone collected from the Moine thrust belt (MTB) exposed on the Sleat Peninsula of Skye, Scotland (Fig. 1, NG 77852375 or Lat. $57^{\circ} 15' 02''$ N: Long. $05^{\circ} 40' 59''$ W). The sample is a Late Mesoproterozoic arkose comprising detrital Archaean / Palaeoproterozoic feldspars that were deformed during the early Phanerozoic Caledonian orogeny. On Skye, the Torridon Group conformably overlies the Sleat Group and there is no obvious break between the two groups (Sutton and Watson 1964). The sediments of the Stoer Group are separated from those of the Torridon Group by an angular unconformity (Stewart 1966) that may represent a significant time gap based on palaeomagnetic data (Stewart and Irving 1974). Rb-Sr ages of 994 ± 48 and 977 ± 39 Ma from samples from the Torridon Group (Stewart 1982) and Pb-Pb ages of 1199 ± 70 Ma from the Stoer Group (Stewart 1982) are considered to be diagenetic ages that are within error of depositional ages (Turnbull et al. 1996). These age data constrain the deposition of the Sleat Group to be around 1000 Ma.

Sediments making up the Torridonian succession are derived from Lewisian basement (Stewart 1982). A major thermal event (the Laxfordian metamorphism) at *c.* 1700 Ma (Rogers and Pankhurst 1993) is likely to have reset K-feldspar $^{40}\text{Ar}/^{39}\text{Ar}$ ages in the Lewisian basement. Consequently, we consider this to be the upper limit of detrital K-feldspar ages within the Torridonian sediments. The Lewisian has a complex thermal history but the youngest cooling ages so far recorded are around 1100 Ma for Rb-Sr dating of biotite (Cliff and Rex 1989).

Deformation associated with movement on the Moine thrust has been dated as 425 ± 12 (Kelley and Powell 1985) though deformation may have continued as late as 408 Ma (Freeman et al. 1998). Thus, there is a considerable period of time since deformation and a significant gap between post-Laxfordian isotopic closure and deformation. The MTB is

reported to have formed at temperatures of approximately 200°C (Soper and Barber 1982; Johnson et al. 1985), a temperature that corresponds with the closure of K-feldspars with effective grain sizes of *c.* 0.1 to 10 µm.

ANALYTICAL PROCEDURE

The deformation history of the area surrounding the sampling site was established using conventional field techniques. Relationships between structures observed in the field or obtained as a result of geological mapping, were used to constrain the deformation history of the area using the procedure described in Potts & Reddy (1999). In the immediate area of the sampling site, the orientations of all mesoscopic structures present were measured and any relationships between them recorded. A surface on the sample was oriented before the sample was removed (Prior et al. 1987) to enable the orientation of the sample to be reconstructed in the laboratory.

During sample preparation all cuts were made parallel to the principal planes of a bedding-parallel, grain-shape foliation. These planes were XY (parallel to the foliation), XZ (parallel to the lineation but perpendicular to the foliation) and YZ (perpendicular to the foliation and the lineation). Three orientated thin sections were prepared each parallel to one of the principal planes and these were examined using optical microscopy. Several orientated blocks were cut from the sample and these were serially sliced using a Cambridge Instruments annular saw with a 30µm thick diamond edged blade. Each block was given a reference name and each slice a reference number. The orientated slices (approximately 250 µm thick) were mounted on glass slides using Lakeside[®] resin and polished in two stages using 10µm and 1µm diamond pastes on conventional laps. The slices were examined using a reflected light optical microscope and two were selected for further analysis. The abrasively polished

surfaces were prepared for electron microscopy using recirculated colloidal silica (Syton[®]) fluid and a polyurethane lap mounted on a Multipol II polishing machine. This removes mechanically induced lattice distortions (Fynn and Powell 1979; Lloyd et al. 1981). ANC images were obtained using carbon coated slices in a Phillips XL30 SEM. Based on their compositional microstructure several clasts were selected for further study. For each suitable clast, montages of overlapping ANC images (Lloyd and Hall 1981; Lloyd 1987) were prepared. These clasts were examined using OC imaging with sample-normal / beam angles of 70° with three semi-conductor detectors placed below the specimen (Prior et al. 1996). The signal was amplified using a KE Electronics amplifier 2BS3. The slices were uncoated but the edges were painted with conducting silver dag to reduce charging. The OC images were tilt-corrected using Phillips operating software.

Based on their crystallographic microstructure, three feldspar clasts (1680A2-XZ-4b, 1680A2-XZ-4a and 1680A2-XY-0, from here on referred to as Clasts 1, 2 & 3 respectively) were selected for detailed scanning electron microscopy and subsequent $^{40}\text{Ar}/^{39}\text{Ar}$ dating. The selection procedure was based on the ability to relate deformation at the grain scale to the macroscopic deformation recorded and mapped in the field, the mesoscopic scale structures observed in the sampling site and the microstructures observed in thin section. For each of the three clasts overlapping OC image montages (Prior et al. 1996) were prepared. In addition, detailed high-resolution OC images were collected in order to constrain the microstructure of the clasts.

Following the completion of the microstructural studies, each slice was soaked in methanol to dissolve the Lakeside[®] resin. The areas containing the clasts to be analysed by UVLAMP were broken from the rest of the slice. The rock chips were cleaned in an ultrasonic bath for 20 minutes in methanol and then deionised water and individually packaged in aluminium

foil. The rock chips were loaded together with age standards Hb3gr and GA1550 (Renne et al. 1998). The samples were irradiated in two batches. One batch (Clasts 1 and 2) was sent to the McMaster reactor in Canada for neutron irradiation. The second went to the Risø nuclear reactor in Denmark. Irradiation times were Clast 1 and 2, 50 hours, Clast 3, 10 hours. J values for the irradiations were 0.01050 ± 0.00005 for both Clasts 1 and 2 and 0.005265 ± 0.000025 for Clast 3.

After irradiation the samples were loaded (with the microstructurally studied side uppermost) into the UV port of the UVLAMP $^{40}\text{Ar}/^{39}\text{Ar}$ dating system at the Open University, UK. The laser port was baked to 120°C overnight using a heat lamp to remove atmospheric contamination. A 10 Hz pulsed quadrupled Nd-YAG laser ($\lambda = 266 \text{ nm}$), with a pulse length of 10 ns, a beam diameter of $\sim 10 \mu\text{m}$, delivering about 1 mJ per pulse, was rastered over $50 \mu\text{m} \times 50 \mu\text{m}$ regions the K-feldspar for approximately nine minutes. This led to laser pit depths of $c. 20 \mu\text{m}$. A Märzhäuser MAC 4000 computerised X-Y stage, attached to a customised Leica DM microscope, was used to control the laser and view the samples during analysis. OC and ANC montages were used to identify areas for Ar analysis. For Clast 1, analyses of the edges of the clast were made by ablating $c. 200 \mu\text{m}$ trenches approximately $10 \mu\text{m}$ from the observable clast boundaries. To investigate the distribution of Ar away from the boundaries of Clast 1, two series of trench analyses parallel to the clast edge were measured from the rim towards the core (Profiles A & B). Profile A was measured from a small fragment broken off from the parent clast and data trenches were spaced every $15 \mu\text{m}$. Profile A comprises 5 analyses. Profile B had trenches spaced at $15 - 30 \mu\text{m}$ and comprises 22 analyses.

Gas released by ablation was gettered for a total of 10 minutes to remove all active gases (CO_2 , H_2O , CH_4 etc.). Remaining noble gases were equilibrated into a high sensitivity MAP 215-50 noble gas mass spectrometer. The automated extraction and data acquisition system was computer controlled. Representative 10 minute extraction system blank measurements obtained during the experiments were $^{40}\text{Ar} = 9 \times 10^{-12}$; $^{39}\text{Ar} = 2 \times 10^{-14}$; $^{38}\text{Ar} = 3 \times 10^{-14}$; $^{37}\text{Ar} = 7 \times 10^{-13}$ and $^{36}\text{Ar} = 2 \times 10^{-13} \text{ cm}^3 \text{ STP}$. Blanks were run before and after every analysis and these were used to correct the data for background counts. The Ar data was corrected for blanks, mass spectrometer discrimination and nuclear-induced interferences (McMaster $^{36/37}\text{Ca} = 0.000255$; $^{39/37}\text{Ca} = 0.00065$; $^{40/39}\text{K} = 0.0015$, Risø $^{36/37}\text{Ca} = 0.00026$; $^{39/37}\text{Ca} = 0.00067$; $^{40/39}\text{K} = 0.045$).

RESULTS

Deformation history of the study area

A detailed account of the deformation history is given in the supplementary data (eText 1). Here we present a brief summary of this deformation history to enable the correlation of structures at the regional, sample and grain scales.

The study area shows evidence of at least three phases of deformation. Two of these produced foliations that can be observed at the sampling site. The third comprises quartz veins and vein arrays that were not found in or near the sampling site or in hand specimen or thin section. The Lochalsh synformal syncline (LSS) is a regionally significant structure of Caledonian age (Silurian). It closes to the ESE and lies in the footwall to the Moine thrust. The oldest foliation (S_1) is found only on the upper overturned limb of the LSS where it is bedding-parallel. This foliation is often associated with a grain shape lineation (L_1) that plunges towards the SE (Fig. 2). This lineation is similar in orientation to grain shape and mineral

lineations observed in mylonites throughout the MTB (Evans and White 1984; Law et al. 1986) and we infer that the bedding-parallel foliation and lineation are of Caledonian age.

The LSS and S_1 are overprinted by a second foliation (S_2). S_2 is not folded, has a similar orientation on both limbs of the LSS and lies oblique to the axial plane of the fold (Fig. 2). Bedding-foliation intersection lineations (S_0/S_2 and S_1/S_2) lie on a great circle that is similar in orientation to the second foliation (Fig. 2). This pattern of intersection lineations suggests that the second foliation is younger than the LSS.

Sample Petrography

Details of the sample petrography are given in supplementary data files (eText1). To summarise, the sample was collected from the upper, overturned limb of the LSS and records a weak development of both S_1 and S_2 . The sample is a well-bedded arkosic wacke. The dominant clastic components are rounded quartz and feldspar clasts and these are found in a finer grained matrix of quartz, feldspar, chlorite and white mica. In the field, the bedding parallel foliation (S_1) could be clearly seen but the lineation (L_1) could not. However, in thin section both structures could be easily seen. The second foliation (S_2) could be seen in the field and in thin section but it is much weaker than the bedding-parallel foliation and lineation. In all three thin sections, the feldspar clasts display planar, intragranular fractures with a limited range of orientations. Together with their opening directions, these orientations suggest that the fractures are related to the formation of the bedding-parallel foliation (S_1) and associated lineation (L_1). Therefore, we interpret them to be of Caledonian age.

Intragrain Microstructure

The three clasts were selected because they contain different microstructures and appear to have undergone differing amounts of deformation. The microstructure of the clasts is discussed in order of increasing strain.

Microstructure of feldspar Clast 1

The feldspar clast is subrounded and of moderate sphericity. It is grain-supported and formed part of a coarse layer in the sample (see eText1). The clast was seen on the faces of several serial slices indicating an original clast size of 1.60 x 0.89 x 0.86 mm (resolved using optical microscopy). The clast is broken into two fragments (Fig 3a, 3b). The fragments fit back together, show similar microstructures at their common edge that differ from those at the detrital grain boundaries, and the region between the fragments is filled with fibrous quartz and mica. These observations suggest that the two fragments were originally parts of the same clast. In the section analysed, the larger fragment measures 1000 x 900 μm and the smaller one 600 x 600 μm .

The original detrital grain boundary can be seen around the outermost part of the clast (Figs. 3a, 4a). Although the fragments have rotated the "long axis" of the "clast" lies at a small angle to the trace of the bedding-parallel foliation. The grain boundaries next to the main fracture are complex, irregular and are unlike the detrital boundary. Both fragments contain two phases; K-feldspar (85 – 90% by area) and plagioclase. The plagioclase has two forms, which have distinct shapes and associations. (1) A single relatively large irregular area close to the upper part of the clast that is bounded by a smooth contact that is, in places, curved and in other places straight. The contact is decorated by several minor phases (white mica, chlorite,

quartz and an opaque phase) and separates the plagioclase from K-feldspar and the second type of plagioclase. The plagioclase in this area displays lamellar twinning. The contact is interpreted as an original grain boundary formed during primary crystallisation of the igneous rock that provided the source of the sediment. (2) Small highly irregular areas up to 200 μm long but mainly 70 μm in length. The boundaries of these areas rarely contain other phases. The areas do not display twinning at an optical scale. They are similar to patch perthites and are interpreted to have developed by deuteric alteration or albitic replacement of the K-feldspar (Lee and Parsons, 1997)

The detrital grain boundary and many of the patch perthites are cut by a series of fractures which, when the clast is restored to its initial shape, were originally parallel (Fig. 3a & 4a). Two of the fractures (the largest in each of the fragments) contain fibrous quartz and white mica (Figs. 3a & 4a). The fibres are sub-parallel to the trace of S_1 , suggesting that the fractures may have opened as this fabric formed. These fractures define 'domains' of the order of 300 x 300 μm .

The K-feldspar has some microstructures that can only be seen in the OC image (Fig. 3b, 5a & 6a). Discrete boundaries (orientation domain boundaries (ODB)) are defined by changes in greyscale (Fig. 3b) that are summarised in Fig. 5a. These structures are linear and generally cross the large fragment from bottom left to top right. These boundaries appear to be isolated segments. In the left-hand portion of the large fragment an irregular boundary is present that separates K-feldspar of different orientations. The boundary contains straight segments that lie perpendicular to those described above. The orientation of these straight segments and the ODB described above are probably crystallographically controlled.

In the right-hand portion of the large fragment there is another type of boundary showing a marked change in orientation (Fig 3b, 6a). Unlike those described above it is closely associated with plagioclase (cf. Fig 3a, 3b). The amount of angular rotation of the K-feldspar lattice across this boundary has not been quantified. However the boundary is a significant microstructural feature that can be traced for several hundred microns across the feldspar. In detail the ODB comprises relatively straight segments that are parallel to larger scale fractures (Fig 3b, 6a). This suggests the ODB developed at the same time as the fractures and is therefore Caledonian in age. The ODB is marked by a complex microstructure involving intergrown plagioclase and K-feldspar (Fig. 6a). Compositional variations (Fig 3a, 4a) mimic the geometry of the ODB and we interpret the plagioclase to have developed by localised replacement of the K-feldspar along the ODB.

Away from the ODB, Clast 1 has a relatively simple microstructure. Slight mottling may be due to the exsolution of fine scale microperthites but there appear to be few deformation-induced microstructures developed (Fig. 6a). We summarise that although fractured, Clast 1 is internally relatively undeformed.

Microstructure of feldspar Clast 2

The clast was seen in several sections and is 3.75 x 3.00 x 2.00 mm (using optical microscopy). It is well rounded and of moderate sphericity and, with the exception of two small touching clasts, is matrix supported. Its long axis lies parallel to the trace of S_1 . The clast is composed of K-feldspar (60% by area) and plagioclase (40%) (Fig. 4b). There are four morphologically distinct types of plagioclase (Fig. 4b): (1) Two highly irregular areas, one in the upper left and one in the upper right of the clast. The boundaries of these areas are curved on the scale of 100 μm but highly irregular on the scale of 10 μm . Both areas contain

inclusions of mica and other phases. The boundaries are interpreted as original grain boundaries formed during primary crystallisation. (2) Small to large, highly irregular areas of plagioclase. The smaller areas are elongate with long axes trending from lower left to upper right. Some of the larger areas are continuous with the more elongate areas. At high magnifications the boundaries are made of linear segments that lie parallel to other features in the clast. Orientation contrast images show that these areas are albite twinned, with the traces of the twin planes running at a high angle from bottom left to top right. The traces of the twin composition planes lie between 3 and 10 μm apart. These areas have characteristics similar to those of patch perthites (Lee et al. 1995). (3) Narrow (10 - 15 μm) highly elongate (up to 300 μm) areas of plagioclase are common. Their long axes trend gently from upper left to lower right and are locally parallel to a mineral cleavage (revealed during polishing). They are rarely more than 100 μm apart. Coarse irregular lamellae such as these are similar to those ascribed to deuteritic coarsening along pre-existing exsolution lamellae which may be coherent or semi-coherent (e.g. Lee and Parsons 1997) and crystallographically controlled. (4) Plagioclase also occurs as strongly aligned, high aspect ratio (20:1) areas of 70 μm maximum length and *c.* 3 μm wide. This form of plagioclase (marked as 'micropertthite' in Fig 4b) is very common and they are generally spaced no more than 30 - 50 μm apart. Again these may represent the deuteritic coarsening of pre-existing exsolution lamellae.

All of the microstructures described above are cut by fractures. The fractures are of two types, filled and closed. The large filled fractures define fragments with dimensions of 800 x 600 μm . The closed fractures are more numerous (easily resolved at high magnification) and define fragments of approximately 200 x 200 μm . The filled fractures contain quartz, mica and occasionally calcite and are extensional in character. The closed fractures appear to have significant components of shear displacement. The patterns of opening and displacement

combined with the orientation of fibres in the fractures indicate that they formed during the formation of S_1 . There is OC across the larger, filled fractures, which indicates some component of rotation. A detailed investigation of the fracture history of this clast is presented elsewhere (Potts and Reddy 2000).

Few, if any, ODBs could be resolved in the K-feldspar (Fig. 5b). The only microstructure revealed using OC imaging was lamellar twinning. The twinning is pervasive and the traces of the twin planes lie only 1 - 2 μm apart. The traces lie parallel to those in the areas of exsolved plagioclase described above (2). The fractures are the dominant deformation microstructure of this clast although the twinning may be deformation induced.

Microstructure of feldspar Clast 3

The microstructure of this feldspar clast has been briefly discussed previously (Reddy et al. 1999). It has a well-rounded detrital shape and is of moderate sphericity. The clast is grain supported and forms part of a coarse layer. The feldspar clast has a long axis of 2060 μm with an aspect ratio of 1.6. The long axis lies parallel to the grain shape lineation (L_1).

The clast contains K-feldspar (70-80 % by area) and plagioclase. Within the clast the plagioclase has three different forms which have distinct shapes and associations (Fig. 4c). (1) A single relatively large irregular area at the lower margin of the clast that is bounded by a smooth, curved contact that is decorated by micas and other minor phases. The plagioclase displays lamellar twinning and the traces of the twin lamellae lie at markedly different orientations to those elsewhere within the detrital grain. This area also contains grains of mica. The boundary is interpreted as an original grain boundary formed during primary crystallisation. (2) Moderately large areas of irregular shape up to 300 μm diameter. The

boundaries of these areas are highly irregular on the scale of 10 μm and curved but irregular on a scale of 100 μm and at high magnifications, they appear to be composed of straight-line segments. The contacts rarely contain other phases and two of these areas display fine lamellar twinning. These areas could be the result of either exsolution or albitic replacement (e.g. Lee et al. 1995; Lee and Parsons 1997). (3) Narrow elongate areas up to 50 or 70 μm wide and up to 100 μm long that often display lamellar twinning. The boundaries of these areas rarely contain other phases and they have a similar appearance to those described immediately above. Locally (e.g. in the upper left and lower right portions of the clast) the long axes of these elongate areas are aligned and their orientation may be crystallographically controlled (Fig. 4c). This is partially confirmed by those in the upper left portion of the clast where the boundaries are sub-perpendicular to the traces of the twins within them.

The detrital grain boundary, the primary K-feldspar-plagioclase grain boundary and several of the patch perthites are cut by a series of mineral-filled fractures that divide the clast into 700 x 350 μm areas (resolved using the ANC images) (Fig. 4c). The fractures contain quartz, feldspar, micas and some minor phases. The orientations of the fractures with respect to the clast long axis, their geographical reference and their displacements suggest that they formed synchronously with S_1 . Within each fragment the traces of the twin planes display a single consistent direction. However, the orientation is slightly different in each block indicating that small rotations may be associated with the fractures. This is confirmed by OC imaging across the fractures.

The K-feldspar has a complex microstructure that can only be resolved using OC images (Fig 5c; and Reddy et al. (1999) Fig. 1). Within the fracture-defined fragments, domains with diameters of 60 to 100 μm are defined by changes in OC and internal, finer scale

microstructure. The ODBs are curved and define an irregular mosaic. They are particularly well developed along the detrital grain boundary (right of Fig. 5c). Close to the margins of the larger fragments the ODBs are more common and they enclose smaller areas. The pattern and geometry of these boundaries suggests that they may have formed after sedimentation and after the fractures. Some of these domains have little or no resolvable internal microstructure. However, other domains display a wide range of OC on a scale of less than 10 μm (Fig 6b). At high magnifications these areas display complex polygonal patterns that reflect different lattice orientations. The origins of the ODBs and lattice misorientations are unclear. They may be the products of crystal plastic deformation. This is supported by the curved, irregular shapes of the ODB and by the presence of smooth, undulose extinction within the highly deformed feldspar. However, discrete linear features (in 2D) show offsets of earlier developed ODBs (Fig. 6b) and suggest that microfaults are pervasively developed throughout the feldspar. The microfaults are in the order of 1 μm wide, are spaced at the 20 μm scale and have separations in the plane of the section of up to 20 μm (Fig 6b). These microstructural features contrast the K-feldspar microstructure seen in the undeformed lattice of Clasts 1 (Fig 6a) and 2.

Argon Isotope Data

The spatial distribution of apparent ages is illustrated in schematic diagrams of the clasts, which show both the locations of each analysis and the feldspar microstructure identified by OC imaging (Fig. 5). The original data are also available as supplementary electronic material (eTables 1, 2 & 3). In all cases the errors (quoted at 1σ) on individual apparent ages are relatively large (mean of 27 Ma) because of the small volumes of material analysed. The K-feldspars show significantly different ranges in apparent ages with an overall decrease in

apparent age with increasing internal deformation (Fig. 7). In each K-feldspar, the spatial distribution of apparent ages is also different (Fig. 5).

Argon isotope data from feldspar Clast 1

Clast 1 is the least deformed K-feldspar and records the largest range of apparent ages (1030 to 357 Ma). There is a systematic distribution of apparent ages within the feldspar with the oldest preserved near the core of the large fragment. The youngest apparent ages are found in the smaller fragment of feldspar. Apparent age distributions around the margins of the clast (Fig. 5a) record a range of ages from 577 to 380 Ma, the youngest being associated with the fractured boundary (414 to 380 Ma). The apparent age distributions within the large fragment of Clast 1 are broadly concentric and are parallel to the clast margins. However, there are two notable departures from this pattern. Firstly, a 200 μm wide band of apparent ages of less than 550 Ma adjacent to the fractured grain edge, in contrast to the rest of the fragment, which yielded apparent ages greater than 550 Ma. Secondly, close to the top of the large fragment, several laser pits gave old apparent ages (707, 749 and 818). ANC imaging (Figs. 3a & 4a) and examination of the volumes of ^{39}Ar and the $^{37}\text{Ar}/^{39}\text{Ar}$ ratio (eTable 1) suggest that these older apparent ages correspond to mixed alkali feldspar - plagioclase analyses. The effect of analysing plagioclase can be seen in the apparent age pattern around the clast edge. Laser trenches that encounter moderately large patches of plagioclase tend to yield older apparent ages. Similarly, the large patch of plagioclase near the top right of the fragment gave an apparent age of 928 Ma (Fig 5a). The larger errors associated with these analyses reflect the low potassium content of the plagioclase. The increased apparent ages may indicate that the plagioclase has not undergone the same degree of resetting as the K-feldspar and therefore has a higher apparent closure temperature than K-feldspar. This might be expected because large areas of plagioclase are usually devoid of the complex microstructures common in K-

feldspar (e.g. Lee and Parsons 1997). Alternatively, the plagioclase ages may suggest the presence of an excess ^{40}Ar component. In this case, the higher apparent ages in plagioclase, relative to those in K-feldspar, would be consistent with a higher excess Ar to radiogenic argon ratio in the plagioclase because of its low K content (e.g. Reddy et al. 1997).

Around the fractured areas of the clast, apparent ages are generally younger and there are no systematic spatial patterns of apparent ages within the clast (Fig 5a). However some of the apparent ages (412, 427 and 432) correspond to analyses of the ODB.

The distribution of apparent ages in profiles A & B (located in Fig 5a and correlating with analyses 26 to 30 and 32 to 52 of eTable 1) are illustrated in Fig. 8. In profile A, all apparent ages were similar and within error (c.460 Ma). They are also of the same order as those within the same part of the clast. In profile B, a progressive increase was seen from the edge of the K-feldspar (533 Ma) towards the centre (900 Ma) (Fig. 8). The apparent age closest to the K-feldspar rim in Profile B is similar to others around the detrital grain boundary.

Argon isotope data from feldspar Clast 2

The range of apparent ages preserved in Clast 2 is much smaller than in Clast 1, is generally lower (480 - 389 Ma) and almost all analyses are within error, with most of the data clustering around 420 Ma (Fig 5b; eTable2). A weighted mean of all the data yields an apparent age of 423 ± 7 Ma. The spatial distribution of data from Clast 2 does not show any clear relationship between position and apparent age (Fig. 5b).

Argon isotope data from feldspar Clast 3

Clast 3 shows a range of apparent ages from 453 to 317 Ma. The distribution of apparent ages within this K-feldspar has been discussed previously (Reddy et al. 1999). To summarise, there

is no clear relationship between apparent age and distance from the clast margin, and there is no evidence for the formation of diffusion profiles over the scale of the clast. Different microstructural domains, recognised by OC imaging, show no discernible apparent age variation and range from 394 to 334 Ma. However analyses of the feldspar across ODBs and fractures yield apparent ages ranging from ca. 450 to 410 Ma, suggesting the presence of an extraneous Ar component in these sites. The source of this Ar is not clear and both an external derivation and trapping of local Ar, formed by radioactive decay within the feldspar, are possible explanations. Two laser ablation trenches adjacent to a fracture surface yield apparent ages of 419 Ma (edge analysis) and 353 Ma. The older apparent age at the fracture surfaces are consistent with diffusion of ^{40}Ar into the feldspar or the trapping of ^{40}Ar in pores developed during fracturing.

DISCUSSION

Sample History, Microstructure and $^{40}\text{Ar}/^{39}\text{Ar}$ Apparent Ages

Detailed geological mapping integrated with meso- and microstructural analyses allows us to confidently relate the deformation history of the feldspar clasts to the regional structural history of the study area. Fractures that affect the feldspar clasts have orientations and displacements consistent with them having developed during the formation of S_1 . In the most deformed clast (Clast 3) variations in lattice orientation, identified by OC imaging, post-date the detrital grain boundaries and are pinned by the S_1 -related fractures. This indicates that the orientation domains recognised in Clast 3 developed during or after S_1 . S_1 is related to deformation associated with the development of the Caledonian MTB. Previous studies in the MTB have constrained deformation to c. 430 - 410 Ma (Kelley 1988; Freeman et al. 1998). These studies provide independent estimates of the age of deformation within the sample.

The feldspars in the sample are all detrital grains derived from a Lewisian precursor and would therefore have had similar cooling ages to other Lewisian K-feldspars. Unfortunately, there are no published K-feldspar $^{40}\text{Ar}/^{39}\text{Ar}$ ages from the Lewisian basement. K-Ar and Rb/Sr cooling ages for Lewisian biotites, range from 1500 Ma to *c.* 1100 Ma depending upon their location within the Lewisian basement (Cliff and Rex 1989). The spatial distribution of apparent ages in Clast 1 and the preservation of *c.* 1000 Ma apparent ages in the clast core suggest that the apparent closure temperature (at the grain scale) was significantly higher than deformation temperature. Apparent ages obtained from the core of Clast 1 are close to the inferred 'closure age' of the feldspars during original cooling. If this is correct, a 40% Ar loss from Clast 1 is required since *c.* 1050 Ma ago to account for the observed apparent age distribution. Originally older 'closure ages' would imply a greater degree of Ar loss. In contrast, apparent ages recorded in the most deformed clast (Clast 3) are younger than the regionally constrained deformation age (*c.* 430 Ma), suggesting that Ar loss took place below the deformation temperature. Both Clasts 2 and 3 require significantly larger degrees of Ar loss than Clast 1.

The three clasts analysed have undergone different degrees of deformation but identical post-sedimentation thermal histories. However, the apparent ages obtained from the K-feldspars are markedly different with the least deformed clast (Clast 1) recording older apparent ages than the most deformed clast (Fig. 7). Microstructural information from Clast 2 shows that the clast is deformed by a complex array of fractures spaced at <100 μm (Figs. 4b & 5b). Similarly, finer scale microstructures are seen in Clast 3 (Fig 6b) and these correlate with even younger apparent ages. In contrast, Clast 1 shows few such features and retains old apparent ages in the core of a fragment defined on one margin by a fracture (Fig. 5a, 6a). These features indicate a correlation of apparent age and grain-scale deformation.

In detail the data show complex relationships between apparent age distributions and microstructural site. The location of the oldest apparent ages in the core of the largest fragment rather than at the centre of the original (unfractured) clast suggests that Ar loss post-dates fracturing. As we have clearly established the links between clast, sample and regional deformation, we can conclude that the Ar loss must be younger than *c.* 430 Ma. This is consistent with the expected timing of heating that would occur due to burial of the sample beneath the hangingwall of the MTB.

Volume diffusion, Multiple Diffusion Domains and Alteration Microstructures

There are strong indications of domains of different orientation below the resolution of the laser (50 μm) in Clasts 2 and 3 (Fig. 6b) and these may reflect small diffusion domain sizes. In contrast, the concentric age distribution in Clast 1 (Fig. 5a, 8) might be interpreted as resulting from volume diffusion in a single crystal. To test this hypothesis, we have undertaken extensive modelling of the age distribution assuming a range of initial core ages from 1000 to 1500 Ma (detail not described here). In so doing we reproduced much of the age distribution with heating events of between 325°C and 360°C during thrust movement at 430 Ma. However, all models failed to reproduce ages within the outermost 200 μm of the detrital grain surface. The volume diffusion profiles could be forced to yield a better fit but only by evoking a 520 Ma heating event. There is no known event of this age in the studied area and we conclude that Clast 1 can not be modelled as a single diffusion domain undergoing volume diffusion.

An alternative model for the concentric apparent age pattern of Clast 1 is a variable, but systematic, distribution of diffusion domain sizes. In this model, smaller diffusion domains at the clast margins would yield younger ages. Larger diffusion domains at the centre of the clast would lead to older apparent ages. We have modelled such a distribution of diffusion

domain sizes for heating at 430 Ma. Our results show that diffusion domain sizes of *c.* 7 μm at the margin, increasing to around 25 μm in the core, would produce the observed apparent age distribution for a 10 Ma heating event of 200°C at 430 Ma. Despite the apparent success of this modelling, there are two fundamental flaws in this approach. Firstly the result is extremely susceptible to small variations in diffusion domain size. For example, a variation from 5 μm to 10 μm at the clast edge would yield ages ranging from 430 Ma to 664 Ma. We can think of no process that would lead to the uniform size of diffusion domains required to explain the consistent edge apparent ages. Secondly, if uniform diffusion domains were present it would be unlikely that these diffusion domains would have the same crystallographic orientation, yet OC imaging (e.g. Fig. 6a) did not reveal any crystallographic misorientations around Clast 1 boundaries. Therefore, we conclude that the apparent age distributions do not reflect a simple model of variably sized diffusion domains within the feldspar.

A final possible explanation for the apparent age distribution seen in Clast 1 is the apparent age pattern reflects the heterogeneous distribution of coherent cryptoperthites and patch perthites that developed during the weathering and transport of the clast into a sediment (I. Parsons, pers. comm. 2000). In such a model, the coherent cryptoperthites would preferentially retain Ar and would be found at the core of the large feldspar fragment while patch perthites would correspond to areas that gave young apparent ages around the feldspar rim. To test such a model requires sub- μm observations (e.g. Lee and Parsons 1998) and the scale of our microstructural observations are not sufficiently fine-scale to achieve this. However, a prediction of this model is that the formation of cryptoperthite and patch perthite would predate the formation of the fractures. This is inconsistent with the observation that the

oldest apparent ages are found at the core of a fragment, which is in part defined by a fracture, rather than at the core of the original sedimentary clast.

The three analysed K-feldspars undoubtedly have a complex microstructural evolution associated with the igneous and metamorphic history of the original protolith (e.g. Lee et al. 1995; Lee and Parsons 1997) and subsequent erosion, redeposition and diagenesis during sedimentation (e.g. Lee and Parsons 1998). However, it is also likely that the three K-feldspars had similarly complex histories that resulted in these processes developing similar microstructural complexities at the grain scale. This is seen in the development of plagioclase on a scale of 10-200 μm that is interpreted to be both the result of exsolution, subsequent coarsening and/or replacement associated with patch perthite formation. It is also apparent that these different types of perthite are thought to have different effects on the diffusion characteristics of K-feldspar; those with semi-coherent to incoherent interfaces potentially having a significant affect on Ar diffusion (Burgess et al. 1992; Parsons et al. 1999). In this study, the coincidence of $^{40}\text{Ar}/^{39}\text{Ar}$ apparent age distributions with deformation-induced microstructures indicates that deformation-related microstructures played a more important role in controlling Ar isotope systematics than did microstructures developed during earlier subsolvus cooling, deuteric alteration and chemical reaction.

Deformation-Related Microstructure and $^{40}\text{Ar}/^{39}\text{Ar}$ Apparent Ages

The correlation of increasing deformation with younger apparent ages indicates that Ar loss from the feldspars is correlated with increasing microstructural complexity. The characteristics of the apparent age distributions amongst the different K-feldspars are consistent with deformation being an important control on Ar systematics. This further suggests that the development of fractures and orientation domains result in a decrease in

diffusion domain size, a change in the diffusion properties of the feldspar, the development of sites of subsequent preferential alteration, or a combination of these.

The distribution of ages around the edges of the K-feldspars should yield information regarding the timing of Ar loss. However, apparent ages at the detrital and fractured grain edges differ in Clast 1. The detrital grain boundaries in Clast 1 record apparent ages (average *c.* 520 Ma) that are older than the fractured boundary analyses. Since the spatial resolution of the laser analyses is the same at both types of site, there must be a difference in the diffusion characteristics of these different microstructural sites. In addition, the small range of apparent ages found throughout the two smaller fragments, and the constant apparent ages in Profile A of Clast 1 (Fig. 8), suggest that diffusion domains in these areas must be of the same size and smaller than the scale of the analyses. If they were larger we would expect to detect age variations towards the edges of the domains. Importantly, the detrital edge analyses (*c.* 520 Ma) do not correlate with any known thermal or geological event. The >430 Ma apparent ages from detrital edges of Clast 1 therefore require further explanation.

There is evidence of a possible excess or trapped ^{40}Ar component in some of the K-feldspar analyses. This is most clearly seen in Clast 3 where the microstructures corresponding to changes in the orientation of the mineral lattice within the K-feldspar yield the oldest apparent ages. Two trench analyses from Clast 3 indicate that an additional ^{40}Ar resides within a 10 μm zone adjacent to the analysed fracture surface. The coincidence of slightly older apparent ages with ODB and fractures surfaces indicates that these microstructural features are either pathways for the migration of externally derived ^{40}Ar or are sites where internally-derived, radiogenic ^{40}Ar may be trapped. Unfortunately, the resolution of the UVLAMP system does not enable us to constrain whether the additional ^{40}Ar adjacent to the fracture surface entered the feldspar by a volume diffusion process or is trapped within much fine-scale

microstructures associated with a fracture damage zone or deuteric alteration. Such a damage zone would be expected to have different diffusion characteristics from the undeformed feldspar structure. If a zone of damage is present at the atomic scale then our data show that it does not appear to extend for distances greater than c. $10\mu\text{m}$ away from fracture surfaces. Similar arguments may be applied to the data from the ODB. We are again unable to constrain whether the additional ^{40}Ar in these zones resides within a discrete and localised ODB or a wider zone of damage/alteration with different diffusion characteristics from the undeformed feldspar lattice. However, the absence of significant diffusion of this ^{40}Ar into the K-feldspar, suggests that these sites are associated with more rapid diffusion of Ar along these pathways.

The above data show that an additional ^{40}Ar component was incorporated into deformation-induced microstructures after significant Ar loss had occurred. It is tempting to speculate that an additional ^{40}Ar component may explain the geologically unreasonable apparent ages (c. 520 Ma) at the margins of Clast 1. However, if this is the case, the addition of ^{40}Ar to Clast 1 edges occurs over a significantly larger scale ($>50\mu\text{m}$) and introduces a higher concentration of excess Ar than associated with the deformation-induced microstructures of Clast 3.

Although this distance is inconsistent with a volume diffusion model, we can not rule out the possibility that a trapped excess ^{40}Ar component has been introduced along microstructures associated with the formation of dislocations and microfractures, deuteric alteration and diagenesis (Parsons et al. 1999). If this scenario is correct, it would explain why the ages at the detrital grain boundaries do not correspond to the time of K-feldspar closure.

Implications for $^{40}\text{Ar}/^{39}\text{Ar}$ dating

By directly observing and analysing microstructures in three deformed K-feldspars, we have demonstrated the existence of a complex series of relationships between deformation-related

microstructures and Ar isotope systematics. A clear relationship is seen with more deformed K-feldspar recording younger apparent ages. However, despite the fact that apparent age distributions are clearly related to deformation-related microstructural evolution, in detail the relationships between Ar diffusion and deformation are not simple.

The role of deformation is to modify both the size and distribution of feldspar domains but it may also alter diffusion characteristics of the feldspar lattice. Deformation is commonly heterogeneous at a range of scales and will be accommodated by a number of different deformation mechanisms that result in a multiplicity of different microstructures. Each of these mechanisms will operate at different rates, will have different length scales and diffusion characteristics and may therefore have profoundly different implications for Ar diffusion. Consequently, the apparent age from a single UVLAMP analysis of deformed K-feldspar (e.g. Clast 3) is likely to represent a mixture of argon components from reservoirs and pathways with varying diffusion characteristics. Although we speculate that this will generally be the case, the data to support this do not currently exist and it remains to be seen how the different microstructures compare at the sub- μm scale. We conclude that microstructural modification during deformation has a significant and complex effect on the diffusion properties of the K-feldspars. Fundamentally, our data show that deformation-related microstructures are significant in controlling grain-scale Ar diffusion in K-feldspars even at low strains.

The deformation outlined in this study took place at conditions within the closure window of Ar diffusion and microstructures would have been forming while diffusion was active. This compromises one of the fundamental assumptions of all closure temperature modelling (Dodson 1973) and the interpretation of cycle heating experiments by MDD modelling

(Lovera et al. 1997). We have shown that deformation, even at low strains, significantly affects the domain structure and diffusion characteristics of K-feldspar and will affect the interpretation of argon release from step heated samples. Given the multitude of different microstructures that may develop in K-feldspar over a range of temperatures, it appears that MDD modelling of $^{40}\text{Ar}/^{39}\text{Ar}$ data from deformed K-feldspars is fundamentally flawed and is unlikely to reproduce the actual thermal history of the sample.

The Ar systematics of a deforming feldspar will be dependant upon the development of dislocation, ODB and fracture networks; the continuous evolution of different diffusion domains; the temperature of formation of these microstructures relative to evolving closure temperatures; and the availability of excess ^{40}Ar . However we have illustrated that by detailed field, microstructural and high spatial resolution $^{40}\text{Ar}/^{39}\text{Ar}$ dating the complexities of these effects may be recognised. With further work a better understanding of the controls of deformation on isotope systematics may be developed and this may ultimately lead to the better constraints on absolute deformation ages.

ACKNOWLEDGEMENTS

A Liverpool University Research Development Grant (ADES5Z) and a NERC small grant (GR9/03130) to SMR supported analytical costs for this work. We would like to thank Ian Parsons, Ray Burgess and an anonymous reviewer for very detailed and constructive reviews that helped clarify the arguments presented in this paper. Kay Lancaster is thanked for her assistance and cartographic skills. This paper is Tectonics Special Research Centre Publication No. 115.

REFERENCES

- Aifantis EC (1979) A new interpretation of diffusion in high-diffusivity pathways - a continuum approach. *Acta Metal* 27: 683-691
- Arnaud NO, Eide EA (2000) Brecciation-related argon redistribution in alkali feldspars: An in naturo crushing study. *Geochim Cosmochim Acta* 64: 3201-3215
- Burgess R, Kelley SP, Parsons I, Walker FDL, Worden RH (1992) ^{40}Ar - ^{39}Ar analysis of perthite microtextures and fluid inclusions in alkali feldspars from the Klokken Syenite, South Greenland. *Earth Planet Sci Lett* 109: 147-167
- Cliff RA, Rex DC (1989) Evidence for a "Grenville" event in the Lewisian of the northern Outer Hebrides. *J Geol Soc Lond* 146: 921-924
- Dalrymple GB, Grove M, Lovera OM, Harrison TM, Hulen JB, Lanphere MA (1999) Age and thermal history of the Geysers plutonic complex (felsite unit), Geysers geothermal field, California: a $^{40}\text{Ar}/^{39}\text{Ar}$ and U-Pb study. *Earth Planet Sci Lett* 173: 285-298
- Dodson MH (1973) Closure temperature in cooling geochronological and petrological systems. *Contrib Mineral Petrol* 40: 259-274
- Dodson MH (1986) Closure profiles in cooling systems. *Mat Sci Forum* 7: 145-153
- Dunlap WJ, Weinburg RF, Searle MP (1998) Karakoram fault zone rocks cool in two phases. *J Geol Soc Lond* 155: 903-912
- Evans DJ, White SH (1984) Microstructural and fabric studies from the rocks of the Moine nappe, Eriboll, NW Scotland. *J Struct Geol* 6: 369-389

- Freeman SR, Butler RWH, Cliff RA, Rex DC (1998) Direct dating of mylonite evolution; a multi-disciplinary geochronological study from the Moine thrust zone, NW Scotland. *J Geol Soc Lond* 155: 745-758
- Fynn GW, Powell WJA (1979) The cutting and polishing of electro-optic materials. Adams Kilger London, pp 216
- Harrison LG (1961) Influence of dislocations on diffusion kinetics in solids with particular reference to the alkali halides. *Trans Faraday Soc* 57: 1191-1199
- Harrison TM, Lovera OM, Heizler MT (1991) $^{40}\text{Ar}/^{39}\text{Ar}$ results for alkali feldspars containing diffusion domains with differing activation-energy. *Geochim Cosmochim Acta* 55: 1435-1448.
- Heizler MT, Harrison TM (1991) The heating duration and provenance age of rocks in the Salton-Sea geothermal-field, Southern California. *J Volcanol Geotherm Res* 46: 73-97.
- Johnson MRW, Kelley SP, Oliver GJH, Winter DA (1985) Thermal effects of thrusting in the Moine Thrust Zone. *J Geol Soc Lond* 142: 863-873.
- Kelley SP (1988) The relationship between K-Ar mineral ages, mica grain sizes and movement on the Moine Thrust Zone, NW Highlands, Scotland. *J Geol Soc Lond* 145: 1-10
- Kelley SP, Powell D (1985) Relationship between marginal thrusting and movement on major internal shear zones in the northern Highland Caledonides, Scotland. *J Struct Geol* 7: 161-174

Lai CT, Morrison HM (1970) Dislocation - enhanced diffusion in silver single crystals.

Canadian J Phys 48: 1548-1552

Law RD, Casey M, Knipe RJ (1986) Kinematic and tectonic significance of microstructures and crystallographic fabrics within quartz mylonites from the Eribol and Assynt regions of the Moine Thrust Zone, NW Scotland. Trans R Soc Edinb Earth Sci 77: 99-126

Le Claire AD, Rabinovitch A (1984) The mathematical analysis of diffusion in dislocations.

In: Murch GE, Norwick AS (eds) Diffusion in Crystalline Solids Material Science and Technology. Academic Press Inc. pp257-318

Lee JKW, Aldama AA (1992) Multipath diffusion: A general numerical model. Computers and Geosciences 5: 531-555

Lee JKW (1995) Multipath diffusion in geochronology. Contrib Mineral Petrol 120: 60-82

Lee MR, Waldron, KA, Parsons I (1995) Exsolution and alteration microtextures in alkali feldspar phenocrysts from the Shap granite. Min Mag 59: 63-78

Lee MR, Parsons I (1997) Dislocation formation and albitization in alkali feldspars from the Shap granite. Am Mineral 82: 557-570

Lee MR, Parsons I (1998) Microtextural controls of diagenetic alteration of detrital alkali feldspars: A case study of the Shap conglomerate (Lower Carboniferous), northwest England. J Sed Res 68: 198-211

- Lloyd GE (1987) Atomic number and crystallographic contrast images with the SEM: a review of backscattered electron techniques. *Min Mag* 51: 3-19
- Lloyd GE, Hall MG (1981) Applications of scanning electron microscopy to the study of deformed rocks. *Tectonophysics* 78: 687-698
- Lloyd GE, Hall MG, Cockayne B, Jones DW (1981) Selected area electron channelling patterns from geologic materials: specimen preparation, indexing and representation of patterns and applications. *Canadian Mineral* 19: 505-518
- Lovera OM, Grove M, Harrison TM, Mahon KI (1997) Systematic analysis of K-feldspar $^{40}\text{Ar}/^{39}\text{Ar}$ step heating results: I. Significance of activation energy determinations. *Geochim Cosmochim Acta* 61: 3171-3192
- Lovera OM, Richter FM, Harrison TM (1989) The $^{40}\text{Ar}/^{39}\text{Ar}$ thermochronology for slowly cooled samples having a distribution of diffusion domain sizes. *J Geophys Res* 94: 17917-17935
- Mock C, Arnaud NO, Cantagrel JM (1999) An early unroofing in northeastern Tibet? Constraints from $^{40}\text{Ar}/^{39}\text{Ar}$ thermochronology on granitoids from the eastern Kunlun range (Qianghai, NW China). *Earth Planet Sci Lett* 171: 107-122
- Parsons I, Brown WL, Smith JV (1999) $^{40}\text{Ar}/^{39}\text{Ar}$ thermochronology using alkali feldspars: real thermal history or mathematical mirage of microtexture? *Contrib Mineral Petrol* 136: 92-110

- Potts GJ, Reddy SM (1999) Construction and systematic assessment of relative deformation histories. *J Struct Geol* 21: 1245-1253
- Potts GJ, Reddy SM (2000) Application of younging tables to the construction of relative deformation histories (1): Fracture systems. *J Struct Geol* 22: 1473-1490
- Prior DJ, Boyle AP, Brenker F, Cheadle MC, Day A, Lopez G, Peruzzo L, Potts GJ, Reddy S, Spiess R, Timms NE, Trimby P, Wheeler J, Zetterström L (1999) The application of electron backscatter diffraction and orientation contrast imaging in the SEM to textural problems in rocks. *Am Mineral* 84: 1741-1759
- Prior DJ, Knipe RJ, Bates MP, Grant NT, Law RD, Lloyd GE, Welbon A, Agar SM, Brodie KH, Maddock RH, Rutter EH, White SH, Bell TH, Ferguson CC, Wheeler J (1987) Orientation of Specimens: Essential data for all fields of Geology. *Geology* 15: 829-831
- Prior DJ, Trimby PW, Weber UD, Dingley DJ (1996) Orientation contrast imaging of microstructures in rocks using forescatter detectors in the scanning electron microscope. *Min Mag* 60: 859-869
- Quidelleur X, Grove M, Lovera OM, Harrison TM, Yin A, Ryerson FJ (1997) Thermal evolution and slip history of the Renbu Zedong Thrust, southeastern Tibet. *J Geophys Res* 102: 2659-2679
- Reddy SM, Kelley SP, Magennis L (1997) A microstructural and argon laserprobe study of shear zone development on the western margin of the Nanga Parbat Syntaxis, north Pakistan. *Contrib Mineral Petrol* 128: 16-29

- Reddy SM, Kelley SP, Wheeler J (1996) A $^{40}\text{Ar}/^{39}\text{Ar}$ laserprobe study of rocks from the Sesia Zone: Excess argon, argon loss and implications for metamorphic and deformation histories. *J Metamorphic Geol* 14: 493-508
- Reddy SM, Potts GJ (1999) Constraining absolute deformation ages: The relationship between deformation mechanisms and isotope systematics. *J Struct Geol* 21: 1255-1265
- Reddy SM, Potts GJ, Kelley SP, Arnaud NO (1999) The effects of deformation-induced microstructures on intragrain $^{40}\text{Ar}/^{39}\text{Ar}$ ages in potassium feldspar. *Geology* 27: 363-366
- Renne PR, Swisher CC, Deino AL, Karner DB, Owens TL, DePaolo DJ (1998) Intercalibration of standards, absolute ages and uncertainties in $^{40}\text{Ar}/^{39}\text{Ar}$ dating. *Chem Geol* 145: 117-152
- Rogers G, Pankhurst RJ (1993) Unravelling dates through the ages: geochronology of the Scottish metamorphic complexes. *J Geol Soc Lond* 150: 447-464
- Soper NJ, Barber AJ (1982) A model for the deep structure of the Moine Thrust zone. *J Geol Soc Lond* 139: 127-138
- Stewart AD (1966) An unconformity in the Torridonian. *Geol Mag* 103: 462-464
- Stewart AD (1982) Late Proterozoic rifting in NW Scotland: the genesis of the "Torridonian". *J Geol Soc Lond* 139: 413-420

Stewart AD, Irving E (1974) Palaeomagnetism of Precambrian sedimentary rocks from NW Scotland and the apparent polar wandering path of Laurentia. *Geophys J R astr Soc* 37: 51-72

Sutton J, Watson J (1964) Some aspects of Torridonian stratigraphy on Skye. *Proceed Geol Assoc* 75: 251-289.

Turnbull MJM, Whitehouse MJ, Moorbath S (1996) New isotopic age determinations for the Torridonian, NW Scotland. *J Geol Soc Lond* 153: 955-964

Villa IM (1994) Multipath Ar transport in K-feldspar deduced from isothermal heating experiments. *Earth Planet Sci Lett* 122: 393-401

Villa IM (1998) Isotopic Closure. *Terra Nova*, 10, 42-47

Waldron K, Lee MR, Parsons, I (1994) The microstructures of perthitic alkali feldspars revealed by hydrofluoric acid etching. *Contrib Mineral Petrol* 116: 360-364.

FIGURES

Fig. 1. Geological map of the northern highlands of Scotland showing the position of the Moine thrust belt. The inset displays an outline map of Scotland.

Fig. 2. Equal area lower hemisphere stereographic projection of structural data from the 4km² area around the sample site on the northern Sleat peninsula, Skye, Scotland.

Fig. 3. Montages of scanning electron microscope images of Clast 1 (1680A2-XZ-4b) showing a) atomic number contrast and b) orientation contrast. The feldspar is now found in two fragments that are interpreted to have originally been the same clast. In (a)

grey-scale variations show variations in composition. In (b) grey-scale variations are mainly associated with differences in crystallographic orientation. However, the coincidence of different grey-scales associated with the different compositions shown in (a) suggest a minor compositional component in the orientation contrast image shown in (b). See Figs. 4 & 5 for summaries. Rectangle in (b) shows the location of Fig. 6a.

Fig. 4. Interpretations of atomic number contrast images of the three clasts analysed in this study. (a) Clast 1; (b) Clast 2; (c) Clast 3.

Fig. 5 Interpretations of the orientation contrast images of the three clasts analysed in this study. The ages obtained are displayed next to the ablation pits. (a) Clast 1. The arrays of closely spaced parallel lines represent the positions of ablation trenches. The apparent ages obtained from area A and area B are shown in Fig. 8. (b) Clast 2. (c) Clast 3. Two trenches were analysed in this feldspar and they are labelled with the appropriate apparent ages (353 and 419 Ma).

Fig. 6. Orientation contrast images showing: a) detail of orientation domain boundary in low strain feldspar (Clast 1). The orientation domain boundary is marked by the discrete change in grey across the middle of the image and by the presence of small patches with different crystallographic orientations. The orientation domain boundary is also associated with plagioclase (cf. Fig. 3a). Low strain, undeformed K-feldspar forms the mottled dark and light grey areas away from the orientation domain boundary. b) Detail of microstructure in deformed K-feldspar (Clast 3) illustrating a different and significantly more complex deformation-induced microstructure.

Fig 7. Histogram (normalised to the total number of analyses for each feldspar) and cumulative frequency of apparent ages from K-feldspar Clasts 1,2 & 3. The data illustrate a significant decrease in apparent age with increasing deformation.

Fig. 8. Apparent age - distance graphs for areas A & B from Clast 1. See Fig. 5a for the locations of the profiles.

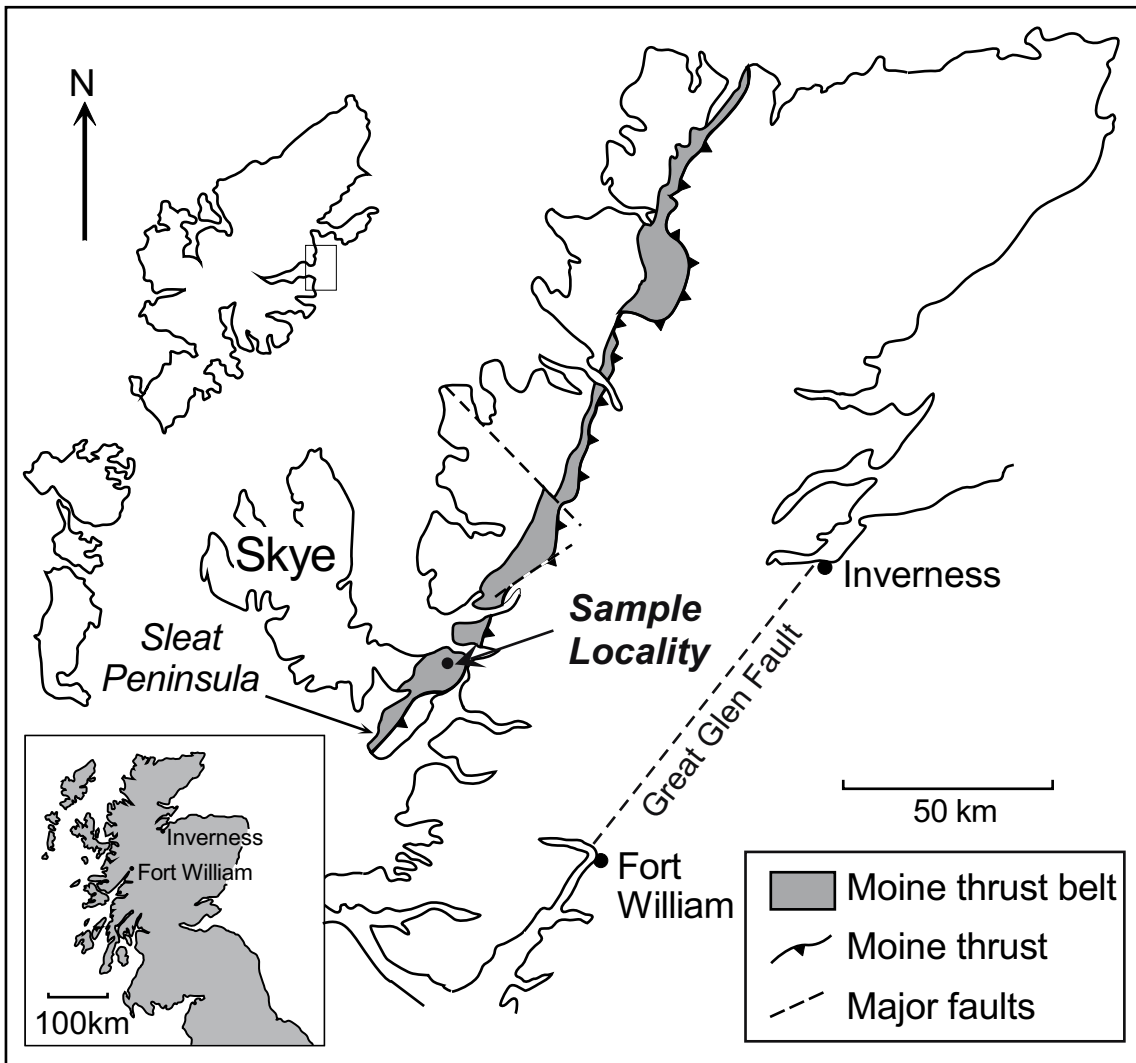


Figure 1

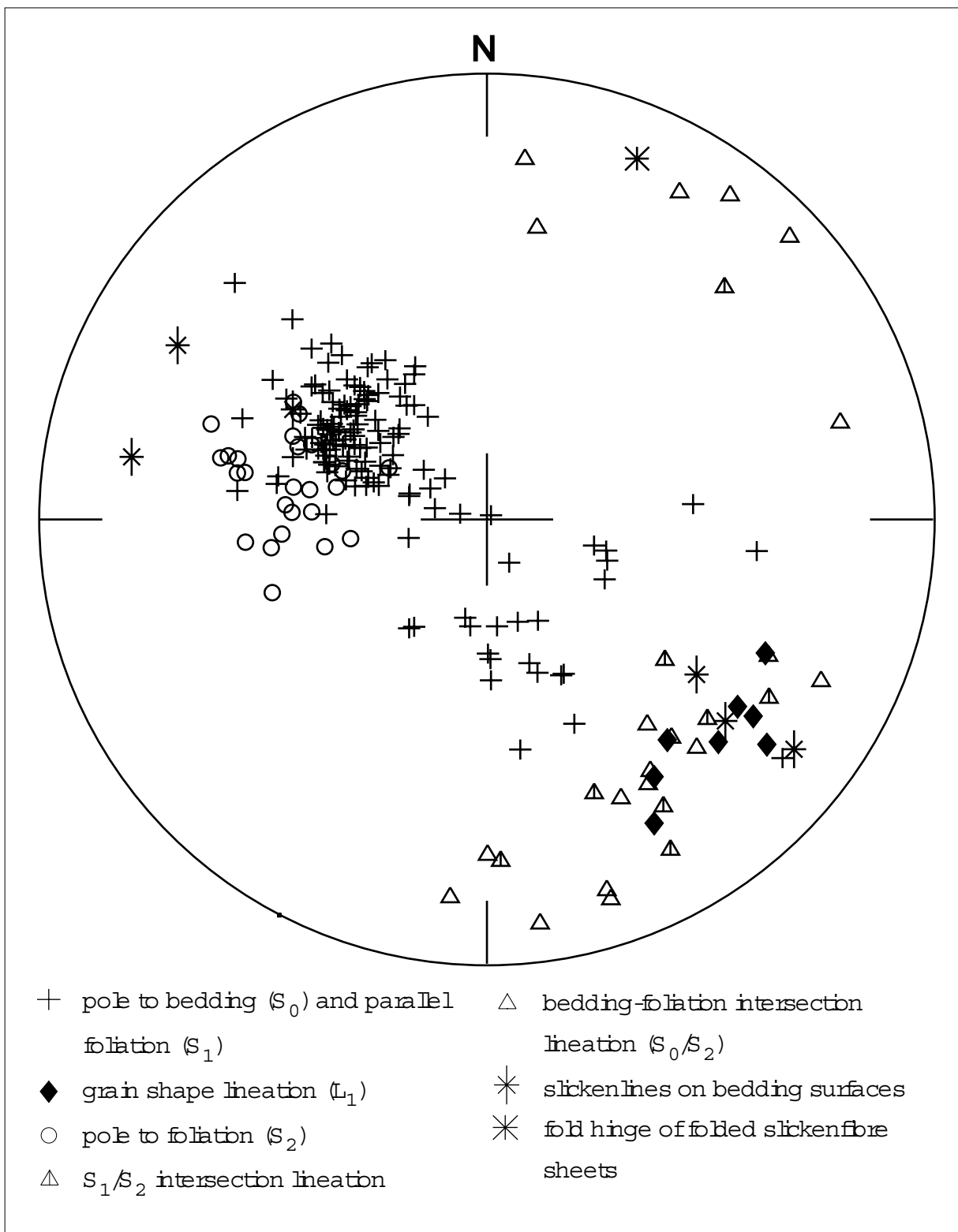
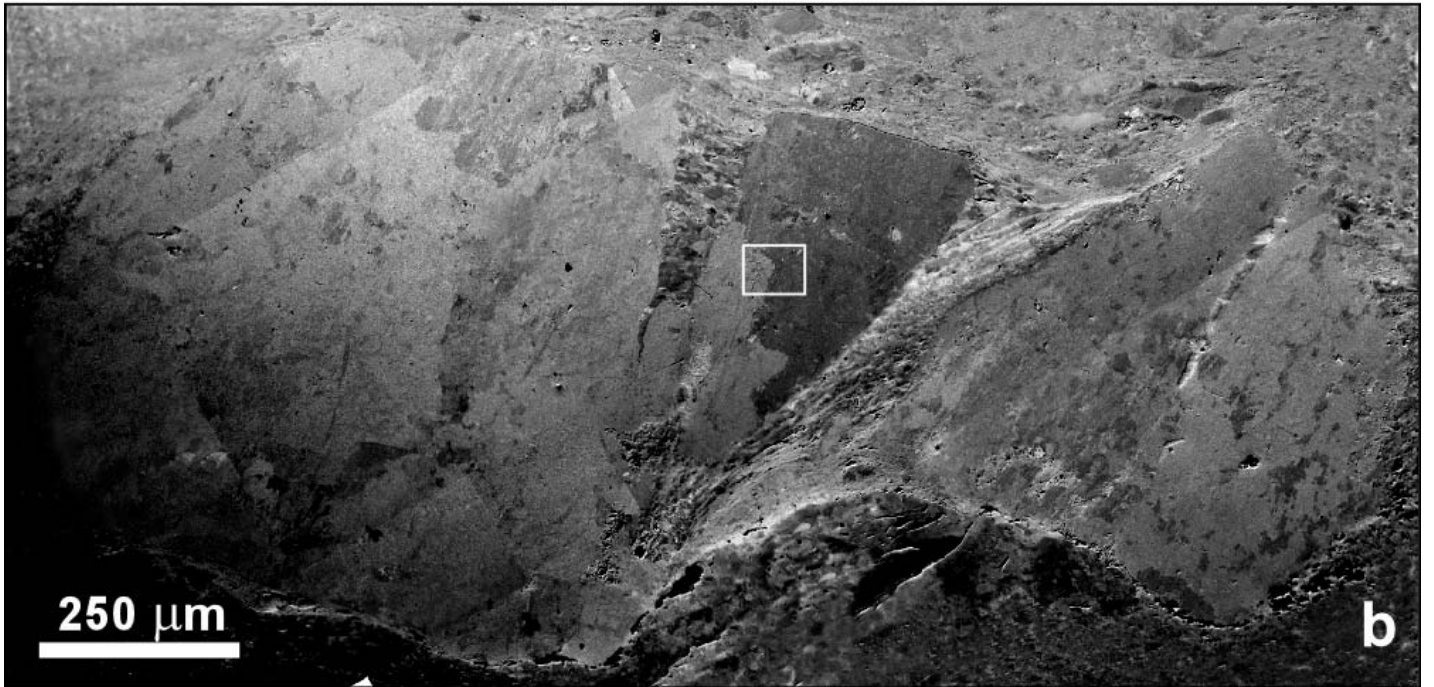
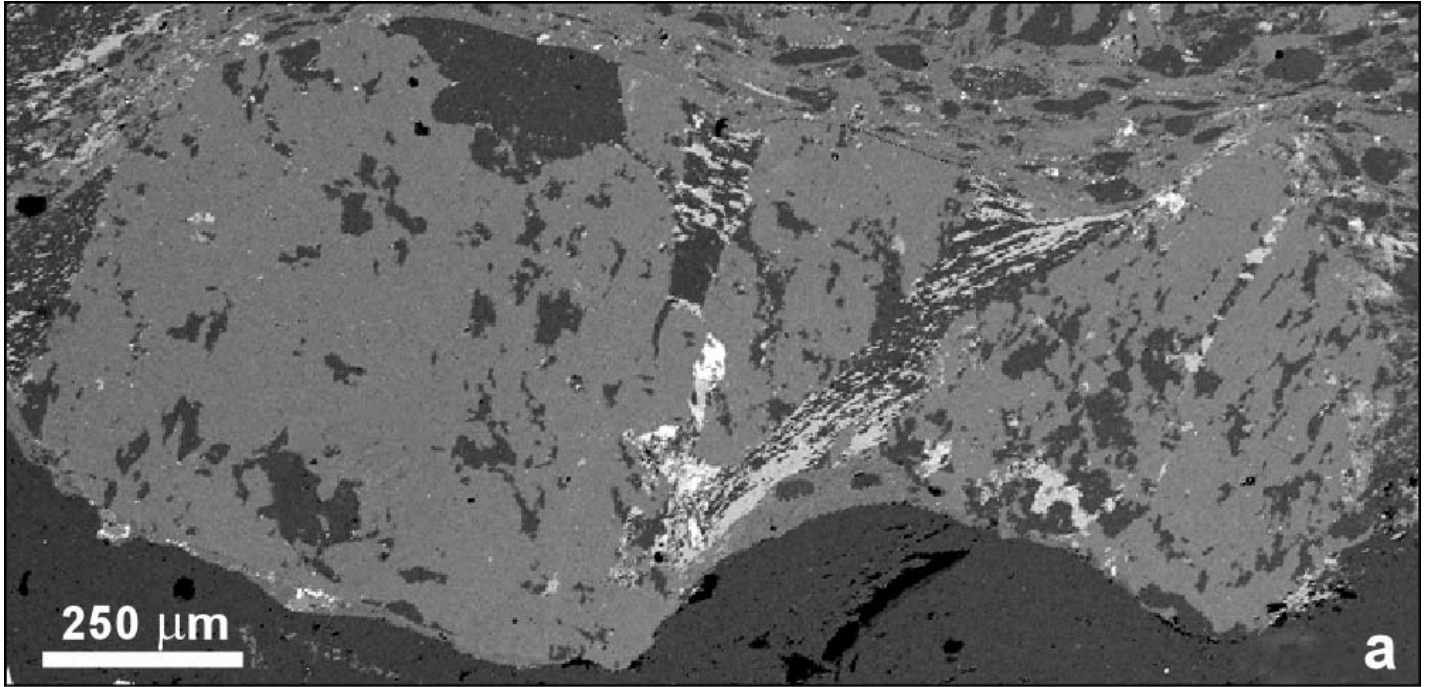


Figure 2



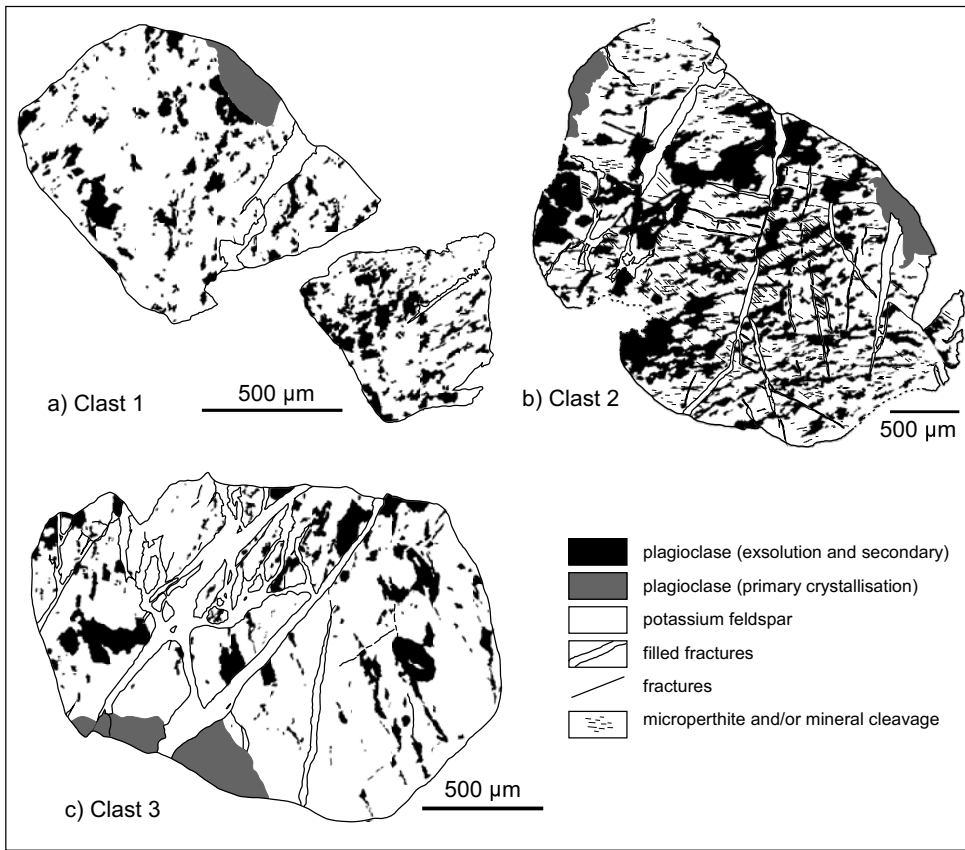
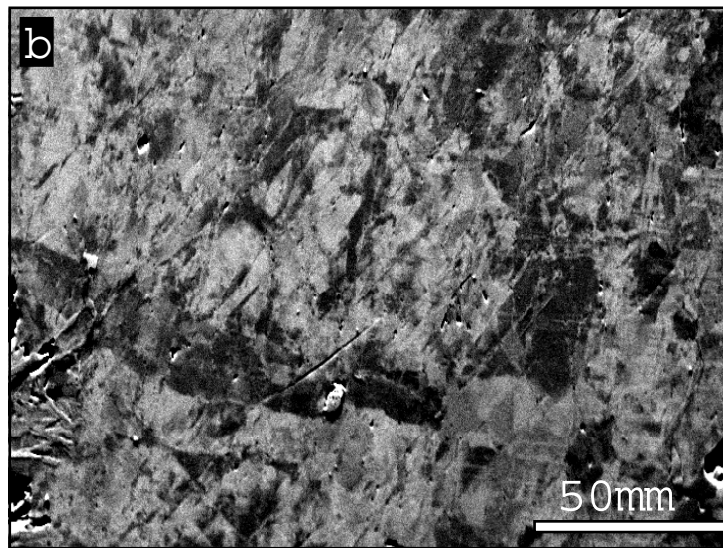
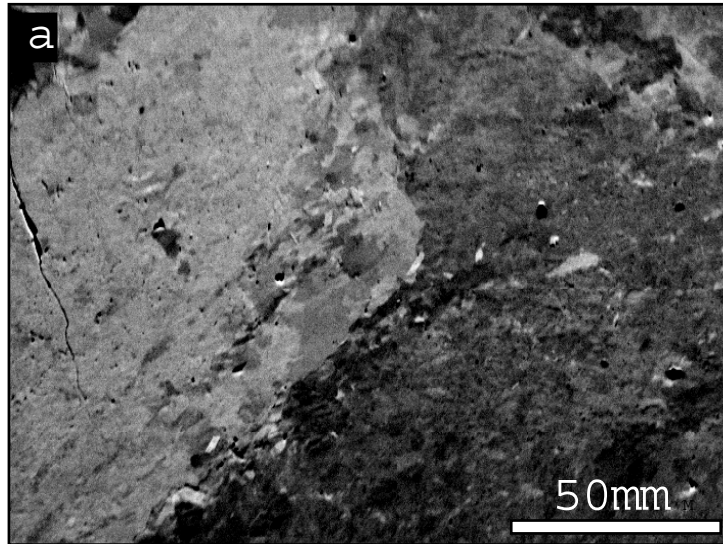
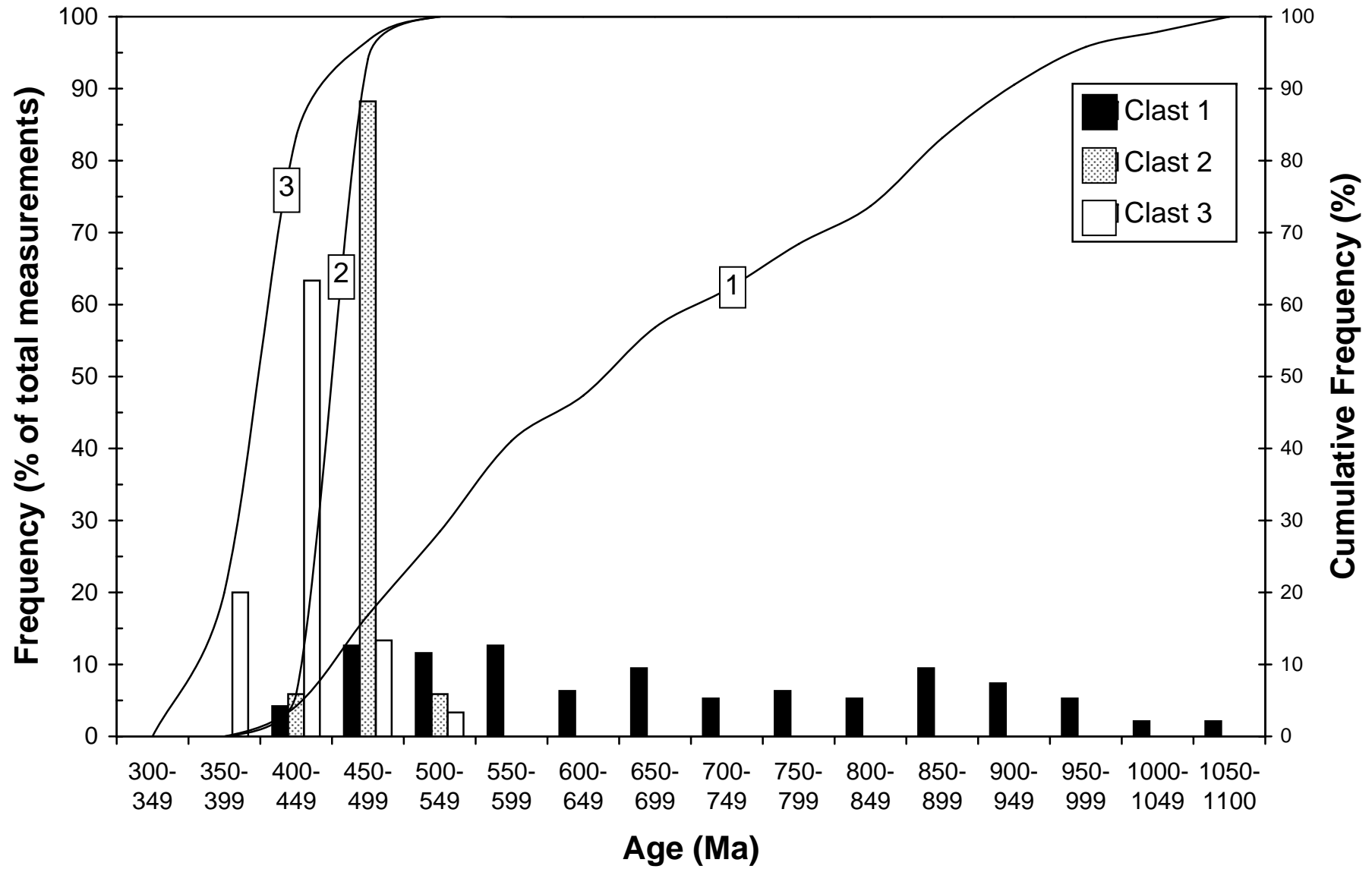
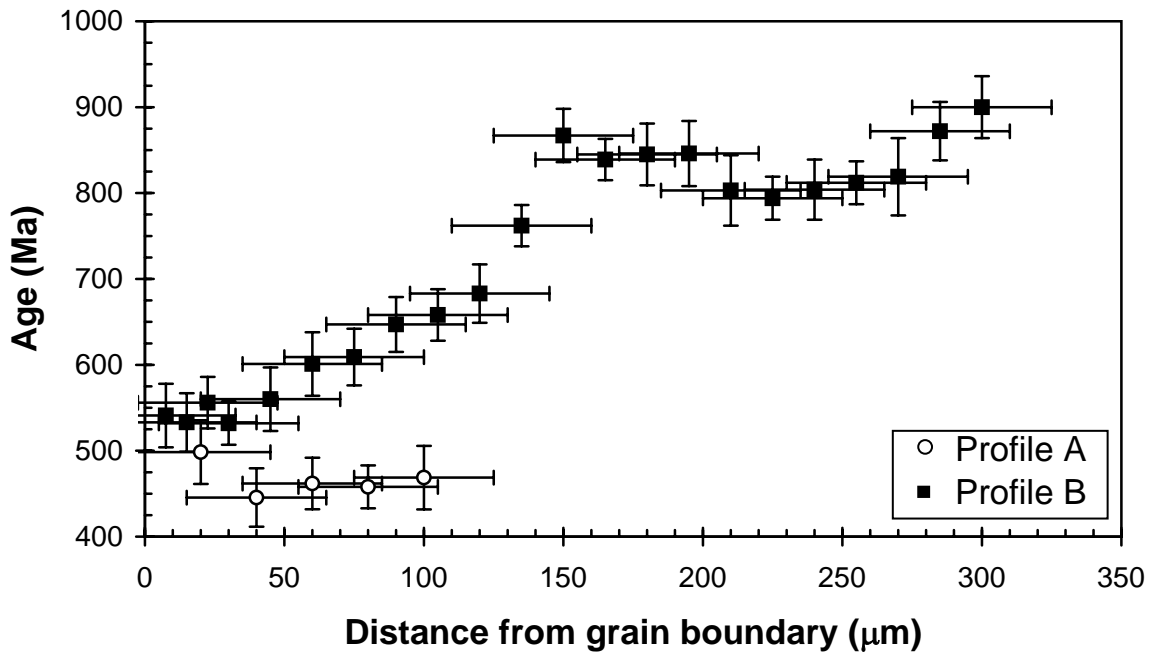


Figure 4

Reddy et al: Figure 6







Supplementary Material (eText 1)

Deformation history of the study area

The Lochalsh synformal syncline (LSS) closes towards the ESE and faces shallowly upwards towards the WNW. The axial surface dips gently towards the ESE but its orientation and position cannot be determined with any accuracy; there are no suitable rock units and insufficient small-scale folds to constrain it. The fold axis is sub-horizontal trending NNE - SSW. Bedding surfaces on both limbs of the fold display slickenlines of various types including slickenfibres, which form parts of bedding-parallel vein systems (Fig. 2). These slickenlines could predate, be synchronous with, or postdate the formation of the LSS (eFig.1). Because they lie in a similar great circle to the poles to bedding (Fig. 2), we infer that they formed at the same time as the fold. However, this is not conclusive.

On the upper, eastern limb of the fold a bedding-parallel grain shape foliation is present (S_1). A marked grain shape lineation is associated with this foliation (L_1). The foliation strikes NNE and the lineation plunges towards the SE. The dip of the foliation and the plunge of the lineation rarely exceed thirty degrees. Both the foliation and lineation become stronger eastwards. Since these structures are restricted to one limb of the fold, it is likely that they formed after the limbs of the LSS became defined i.e. either during or after the formation of the synform (eFig.1). A third possibility, that the foliation and lineation predate the fold (eFig.1), is possible but we consider it unlikely. The cluster of points representing the orientation of the lineation (Fig. 2) lies perpendicular to the fold axis of the LSS. This geometrical arrangement is taken to indicate that the bedding-parallel foliation and associated lineation are the same age as the LSS but this is not conclusive. Also, on the eastern limb of the LSS, where the bedding-parallel foliation and lineation are strong, are arrays of quartz

veins. The internal geometries of the arrays are complex with several vein orientations (not shown). Often the vein fills are fibrous and although the veins display a wide range of orientations the fibres have a consistent orientation parallel to the grain shape lineation in the matrix. The parallelism of these two structures is taken to indicate that these vein systems and the bedding-parallel foliation and associated lineation formed at the same time. The bedding-parallel foliation (and associated lineation) and the slickenlines are found in different parts of the fold and no relationship between them can be established.

A second foliation (S_2) is present which dips at 30-40° towards the E or ESE (Fig. 2). This foliation is present on both limbs of the LSS. Throughout the area, this foliation is oblique to the axial surface of the fold and it dips more steeply than the limbs and the axial surface of the fold. This geometry combined with the consistent orientation of the foliation (i.e. it is not folded) suggests that the foliation is later than the LSS (eFig. 1). This foliation lies parallel to the axial surfaces of small-scale folds of the slicken fibre sheets (Fig. 2) and the bedding-parallel quartz veins, indicating that the foliation is younger than the slickenlines and bedding-parallel veins (eFig. 1). Occasionally, the oblique foliation can be seen to crenulate the bedding-parallel foliation though no direct relationship with the associated lineation could be established. Thus, the oblique foliation (S_2) is younger than the bedding-parallel foliation.

The latest structures to be formed are arrays of quartz veins (eFig. 1) which display a variety of vein and vein array geometries. These variations are not significant in the context of this paper. In both geometry and orientation (not shown) these arrays are different to those described earlier. They are present on both limbs of the LSS and their orientations and displacement patterns are identical on both limbs of the fold indicating that they post-date it. Neither the veins nor the arrays show any kinematic evidence to suggest that they formed

synchronously with the fold. No relationships between the slickenlines and these vein arrays were recorded. However, the vein arrays are not foliated by the bedding-parallel or later oblique foliation, suggesting that they are younger than both of the foliations (eFig. 1). These veins are rarely fibrous but when they are the orientation of the fibres is consistent with the kinematics of the vein array rather than the bedding-parallel foliation and associated lineation.

The sample was collected from a location close to the centre of northern Sleat (Fig. 1). Only two of the structures described above are present at the location from which the sample was taken; the bedding-parallel grain shape foliation (S_1 , but no associated lineation) and the oblique foliation (S_2). Thus, it would appear that the sample location underwent both phases of penetrative deformation.

Sample Petrography

The sample is an arkosic wacke (*sensu* Dott 1964, Pettijohn et al. 1972) which comprises alternating layers of very fine to fine and coarse to very coarse (Udden-Wentworth scale) siliciclastic grains. The layers are 3 to 5 mm thick. The finer layers are indistinguishable from the matrix in the coarser layers. The finer layers, and to some extent the matrix of the coarser layers, are well sorted. Since the coarser layers contain grains ranging in size from very fine (in the matrix) to very coarse they must be classed as very poorly sorted (*sensu* Folk 1974) although, the coarser fraction has a restricted range of grain diameters and may be described as poorly sorted. The sample, as a whole, contains only a very small proportion of grains of medium sand grade thus, the rock has a bimodal grain size distribution. The large grains in the coarser layers are either matrix- or clast- supported and, in thin section, there is no visible porosity.

The dominant clast types are quartz and feldspar. The large feldspar clasts within the coarser layers are rounded to sub-rounded and of moderate to high sphericity and they appear to have retained their detrital shapes. The shapes of the larger quartz grains are more complex and appear to be related to deformation. In the finer layers and in the matrix of the coarser layers the feldspar clasts are of moderate sphericity and, in thin section, they appear more angular than the coarser feldspars described above. Given their moderate sphericity this angularity may be original. The finer quartz clasts have shapes indicative of deformation.

In each thin section the long axes of the clasts of quartz and feldspar display a limited range of orientations. In the XZ and YZ sections (of the bedding-parallel foliation and lineation) the long axes lie parallel to the trace of the bedding (as defined by grain size variations). A marked grain shape lineation can be clearly seen in the XY section (in contrast to the field). Thus, the sample possesses the bedding-parallel foliation (S_1) and associated lineation (L_1).

In thin section, very fine grained ($\ll 0.1\text{mm}$) chlorites and perhaps white micas are found throughout the rock. These phyllosilicates display a strong shape alignment sub-parallel to bedding and foliation except where they wrap clasts of quartz and feldspar. Rare, 0.1×0.05 mm flakes of white mica are present throughout the rock. These grains generally lie with their basal planes sub-parallel to the bedding (S_0) and foliation (S_1) described above.

The feldspar clasts in all three thin sections display planar intra-granular planar fractures. These fractures possess a limited range of orientations, which together with their opening directions suggest that the fractures are related to the formation of the bedding-parallel foliation and associated lineation. Thus, they are of Caledonian age.

In the XZ section one small area rich in phyllosilicates is crenulated. The traces of the axial surfaces of the microfolds are parallel to the trace of the oblique foliation (S_2) in the section plane. The geometry of the folds indicates that the phyllosilicates originally lay parallel to the bedding-parallel foliation. Thus, the thin sections show evidence of multiple deformations and that the oblique foliation formed after the bedding-parallel foliation (eFig. 1), the grain shape lineation and the associated fractures. In the sample, the bedding-parallel foliation and lineation are much stronger than the oblique foliation.

Many of the clasts of feldspar display smooth undulose extinction that is unlike the marked changes in extinction that are associated with the fractures.

eText 1: References

Dott RL (1964) Wacke, greywacke and matrix – what approach to immature sandstone classification? *J Sed Petrol* 34: 625-632.

Folk RL (1974) *Petrology of Sedimentary Rocks*. Hemphill Pub, Austin Texas, pp 182

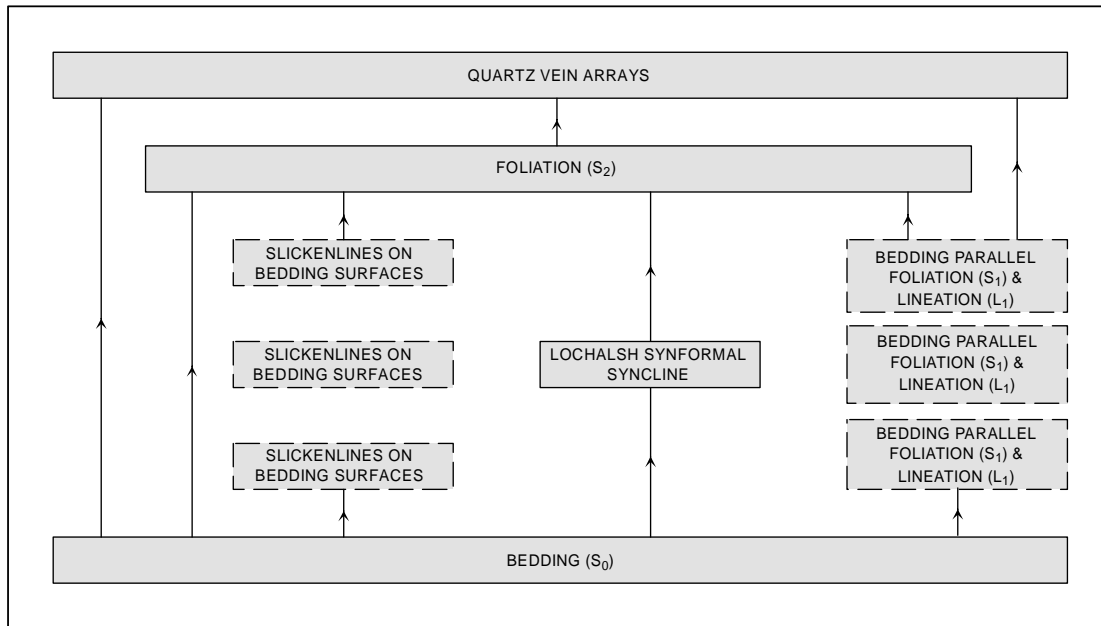
Pettijohn FJ, Potter PE, Siever R (1972) *Sand and Sandstone*. Springer, New York, pp 618

Potts GJ, Reddy SM (2000) Application of younging tables to the construction of relative deformation histories (1): Fracture systems. *J Struct Geol* 22: 1473-1490

Supplementary Material: eFigure Captions

eFig.1. Possible deformation histories for northern Sleat, Skye, Scotland. The oldest event lies at the bottom of the diagram the youngest at the top. The relative positions of the boxes show the relative ages of the structures (or events). Tie lines between the boxes indicate that evidence exists to substantiate the relative ages of the structures. Due to the lack of evidence, the relative ages of some structures cannot be established and they may occur at one or more stage in the deformation history. Such structures are placed in boxes surrounded by dashed lines. For discussion of this approach see Potts and Reddy (2000).

Reddy et al: eFig 1.



Reddy et al: eTable 1

Analysis	⁴⁰ Ar/ ³⁹ Ar	+	³⁸ Ar/ ³⁹ Ar	+	³⁷ Ar/ ³⁹ Ar	+	³⁶ Ar/ ³⁹ Ar	+	⁴⁰ Ar/ ³⁹ Ar	+	³⁹ Ar	+	Age (Ma)	+
Ksp 1	59.69602	0.72323	0.01578	0.00210	-0.00301	-0.00688	0.00000		59.69602	1.43935	0.01535	0.00018	878	37
Ksp 2	33.51097	0.17711	0.01360	0.00244	0.00271	0.00500	0.00000		33.51097	0.81068	0.01704	0.00008	544	25
Ksp 3	30.66889	0.36105	0.01268	0.00093	0.00711	0.00591	0.00110	0.00275	30.34286	0.88641	0.01662	0.00019	499	24
Ksp 4	31.82171	0.37176	0.00864	0.00293	0.01264	0.00834	0.00000		31.82171	1.58729	0.01097	0.00012	520	31
Ksp 5	27.12807	0.37892	0.00984	0.00196	0.00131	0.00723	0.00156	0.00431	26.66811	1.32813	0.01178	0.00015	445	27
Ksp 6	24.43012	0.35459	0.01171	0.00275	0.00132	0.00841	0.00000		24.43012	1.33199	0.01169	0.00016	412	27
Ksp 7	26.95839	0.50245	0.01476	0.00192	-0.00127	-0.00702	0.00398	0.00533	25.78137	1.64657	0.01213	0.00022	432	31
Ksp 8	33.82937	0.42949	0.01475	0.00216	0.00527	0.00986	0.00078	0.00604	33.59942	1.83451	0.01071	0.00013	545	34
Ksp 9	33.44528	0.61304	0.01507	0.00208	-0.00321	-0.00879	0.00000		33.44528	1.47557	0.01118	0.00020	543	30
Ksp 10	25.43828	0.31370	0.01322	0.00238	0.00796	0.00725	0.00000		25.43828	1.04308	0.01355	0.00016	427	24
Ksp 11	29.73986	0.43137	0.00997	0.00138	-0.00741	-0.01080	0.00000		29.73986	0.95771	0.01281	0.00018	490	25
Ksp 12	67.37671	0.53447	0.01211	0.00177	-0.00897	-0.00864	0.00071	0.00264	67.16601	0.94569	0.01402	0.00011	963	37
Ksp 13	63.14814	0.88598	0.01711	0.00183	0.00057	0.00889	0.00000		63.14814	1.19655	0.01362	0.00019	918	37
Ksp 14	46.49124	1.09202	0.00957	0.00223	-0.00668	-0.01186	0.00000		46.49124	1.34465	0.01114	0.00026	717	33
Ksp 15	40.79370	0.66857	0.01215	0.00236	-0.01099	-0.01108	0.00285	0.00433	39.95056	1.43808	0.01051	0.00017	632	32
Ksp 16	38.03186	0.62927	0.01237	0.00260	-0.00817	-0.00905	0.00000		38.03186	1.21993	0.01288	0.00021	606	30
Ksp 17	57.95158	0.60179	0.01318	0.00181	-0.00319	-0.00851	0.00146	0.00216	57.51987	0.87441	0.01369	0.00014	852	34
Ksp 18	24.02181	0.48686	0.00742	0.00215	0.00601	0.01010	0.00087	0.00322	23.76551	1.06553	0.01153	0.00023	402	24
Ksp 19	41.05404	0.86752	0.01111	0.00200	0.00227	0.01062	0.00643	0.00366	39.15488	1.36213	0.01245	0.00026	621	31
Ksp 20	32.13005	0.37523	0.00873	0.00203	-0.00694	-0.00954	0.00655	0.00242	30.19393	0.79833	0.01221	0.00014	497	24
Ksp 21	59.86027	0.96803	0.01064	0.00223	-0.00360	-0.00809	0.00000		59.86027	1.21346	0.01497	0.00024	880	36
Ksp 22	69.85567	0.81624	0.01049	0.00253	-0.00565	-0.00919	0.00607	0.00281	68.06233	1.15108	0.01318	0.00015	973	38
Ksp 23	74.02768	1.21738	0.01323	0.00194	-0.00180	-0.00907	0.00234	0.00355	73.33707	1.59822	0.01284	0.00021	1030	41
Ksp 24	33.61720	0.38390	0.00964	0.00233	-0.00376	-0.00881	0.00000		33.61720	0.85524	0.01434	0.00016	545	25
Ksp 25	56.48187	0.68587	0.00778	0.00337	-0.01138	-0.00669	0.00000		56.48187	1.29366	0.01245	0.00015	840	35
Ksp 26	30.30228	0.30514	0.01640	0.00418	0.02083	0.00983	0.00000		30.30228	1.35586	0.00848	0.00008	498	28
Ksp 27	26.67963	0.52957	0.01259	0.00461	0.00160	0.00492	0.00000		26.67963	1.85132	0.00770	0.00015	446	33
Ksp 28	27.85649	0.22371	0.01507	0.00453	-0.00630	-0.00942	0.00226	0.00590	27.78099	1.75881	0.00783	0.00006	462	32
Ksp 29	27.99597	0.64904	0.01154	0.00474	-0.00659	-0.00985	0.00160	0.00506	27.52207	1.62703	0.00748	0.00017	458	31
Ksp 30	29.20149	0.48200	0.01258	0.00516	0.02871	0.00804	0.00320	0.00552	28.25479	1.69631	0.00687	0.00011	469	32
Ksp 31	33.27523	0.38305	0.00997	0.00207	0.00732	0.00270	0.00000		33.27523	0.75810	0.01712	0.00019	541	25
Ksp 32	32.75047	0.70882	0.01087	0.00397	0.00204	0.01422	0.00000		32.75047	2.75411	0.00630	0.00013	533	45
Ksp 33	34.35577	0.44241	0.00699	0.00369	-0.00265	-0.00740	0.00000		34.35577	1.80713	0.00679	0.00008	556	34
Ksp 34	32.95798	0.30093	0.00835	0.00305	0.01409	0.00881	0.00091	0.00692	32.68771	2.06613	0.00820	0.00007	532	36
Ksp 35	36.26164	0.47508	0.00901	0.00285	-0.00673	-0.00920	0.00541	0.00549	34.66166	1.68484	0.00877	0.00011	560	33
Ksp 36	37.99618	0.49778	0.01329	0.00118	-0.00249	-0.00522	0.00113	0.00260	37.66165	0.91382	0.01546	0.00020	601	27
Ksp 37	38.89533	0.45621	0.00863	0.00204	0.00078	0.00490	0.00227	0.00244	38.22310	0.84936	0.01648	0.00019	609	27
Ksp 38	41.20765	0.51461	0.01110	0.00165	0.00264	0.00396	0.00337	0.00197	41.09898	0.77674	0.02039	0.00025	647	28
Ksp 39	42.85561	0.43027	0.01208	0.00118	0.00300	0.00462	0.00316	0.00188	41.92160	0.69815	0.02136	0.00021	658	28
Ksp 40	44.18492	0.51365	0.01041	0.00155	0.00436	0.00453	0.00126	0.00221	43.81157	0.82878	0.02177	0.00025	683	29
Ksp 41	50.06292	0.83903	0.01162	0.00117	-0.00468	-0.00821	0.00000		50.06292	1.33813	0.01411	0.00023	762	34
Ksp 42	58.74183	0.96297	0.01146	0.00192	-0.00118	-0.00782	0.00000		58.74183	1.61147	0.01248	0.00020	867	38
Ksp 43	57.00578	0.44397	0.01208	0.00257	-0.00196	-0.00859	0.00214	0.00477	56.37453	1.47734	0.01271	0.00009	839	36
Ksp 44	57.42312	0.70148	0.01287	0.00228	0.00184	0.00806	0.00189	0.00379	56.86536	1.31926	0.01438	0.00017	845	36
Ksp 45	57.74867	0.81817	0.01214	0.00166	-0.00530	-0.00646	0.00258	0.00379	56.98542	1.38193	0.01438	0.00020	846	36
Ksp 46	53.55174	0.52669	0.01323	0.00301	0.00042	0.00737	0.00051	0.00433	53.40088	1.38435	0.01399	0.00013	803	35
Ksp 47	53.84222	0.75290	0.01251	0.00235	0.00336	0.00831	0.00410	0.00357	52.63162	1.28641	0.01395	0.00019	794	34
Ksp 48	55.00523	0.91551	0.00865	0.00178	0.00286	0.01257	0.00511	0.00658	53.49390	2.13872	0.00922	0.00015	804	40
Ksp 49	54.11033	0.53606	0.01368	0.00177	-0.00336	-0.00762	0.00000		54.11033	1.30702	0.01353	0.00013	812	35
Ksp 50	54.68034	1.08128	0.01371	0.00331	-0.00519	-0.00767	0.00000		54.68034	1.58261	0.01273	0.00025	819	37
Ksp 51	60.05268	0.38182	0.01309	0.00151	0.00559	0.00654	0.00299	0.00346	59.16829	1.09095	0.01575	0.00009	872	35
Ksp 52	62.36535	0.59227	0.01232	0.00218	0.00176	0.00618	0.00247	0.00404	61.63501	1.32844	0.01503	0.00014	900	37
Ksp 53	48.22184	0.69166	0.01252	0.00209	-0.00128	-0.01015	0.00000		48.22184	1.57217	0.01142	0.00016	739	35
Ksp 54	41.58475	0.88501	0.01159	0.00284	0.01951	0.00782	0.00000		41.58475	1.07455	0.01000	0.00021	654	30
Ksp 55	64.53197	1.24511	0.01316	0.00884	0.02565	0.02879	0.00156	0.01569	64.07059	4.79887	0.00320	0.00006	928	64
Ksp 56	29.97915	0.44973	0.01237	0.00370	0.02546	0.00942	0.00587	0.00526	28.24386	1.61177	0.00766	0.00011	469	31
Ksp 57	59.52649	0.96132	0.01504	0.00239	0.00431	0.00840	0.00000		59.52649	1.22220	0.01191	0.00019	876	36
Ksp 58	46.20053	0.99768	0.01309	0.00641	0.02552	0.01638	0.00000		46.20053	1.88184	0.00563	0.00012	713	37
Ksp 59	39.66529	1.10323	0.01316	0.00196	-0.00441	-0.00756	0.00000		39.66529	1.72640	0.01682	0.00023	628	34
Ksp 60	44.63080	1.18940	0.01202	0.00162	-0.00084	-0.00725	0.00000		44.63080	1.82890	0.01490	0.00017	693	36
Ksp 61	62.54793	1.16607	0.01307	0.00131	0.00375	0.00614	0.00000		62.54793	1.67673	0.01853	0.00023	911	39
Ksp 62	39.44036	1.51532	0.01347	0.00206	-0.00195	-0.01025	0.00000		39.44036	2.52296	0.01173	0.00020	625	42
Ksp 63	25.54638	0.19440	0.01187	0.00254	0.13444	0.08074	-0.00003	-0.00398	25.55651	1.19225	0.01198	0.00007	428	18
Ksp 64	32.23439	0.27539	0.01201	0.00146	0.01335	0.03400	0.00135	0.00184	31.83565	0.60903	0.02587	0.00021	519	9
Ksp 65	37.29046	0.28131	0.01312	0.00155	0.01413	0.03959	0.00183	0.00195	36.74831	0.63912	0.02448	0.00018	587	9
Ksp 66	40.79215	0.81930	0.01720	0.00303	0.23974	0.07179	-0.00006	-0.00472	40.81022	1.61812	0.01010	0.00020	642	22
Ksp 67	49.80896	0.60385	0.01235	0.00152	-0.01152	-0.03296	0.00225	0.00198	49.14456	0.83523	0.02004	0.00024	749	11
Ksp 68	65.47847	0.52261	0.01496	0.00190	-0.00951	-0.03631	0.00062	0.00196	65.29532	0.77986	0.02430	0.00019	940	9
Ksp 69	60.43261	0.60707	0.01191	0.00156	-0.01001	-0.04425	0.00000	0.00163	60.43185	0.77579	0.02105	0.00021	884	10
Ksp 70	75.06644	1.02766	0.01137	0.00192	0.09133	0.04228	0.00605	0.00156	73.27782	1.10431	0.02205	0.00030	1027	12
Ksp 71	49.89024	1.03871	0.00992	0.00224	0.08186	0.03953	-0.00002	-0.00182						

Analysis	$^{40}\text{Ar}/^{39}\text{Ar}$	+-	$^{38}\text{Ar}/^{39}\text{Ar}$	+-	$^{37}\text{Ar}/^{39}\text{Ar}$	+-	$^{40}\text{Ar}^*/^{39}\text{Ar}$	+-	^{39}Ar	+-	Age (Ma)	+-
Ksp 1	26.23900	2.04219	0.01340	0.00306	0.00493	0.01710	24.77725	3.80663	0.78616	0.00803	417.2	59.9
Ksp 2	26.09692	0.98507	0.01106	0.00182	0.00214	0.00568	26.09692	1.63668	1.81005	0.03001	436.9	30.6
Ksp 3	25.39322	1.14403	0.01453	0.00116	0.00621	0.00785	24.80465	1.91686	1.45040	0.01802	417.6	33.8
Ksp 4	24.42365	1.19521	0.01078	0.00240	0.00058	0.00879	24.42365	2.02276	1.36831	0.01502	411.9	35.2
Ksp 5	22.91504	0.76818	0.01319	0.00153	0.00847	0.00528	22.91504	1.47323	2.15567	0.01702	389.0	28.0
Ksp 6	29.02257	0.78764	0.01282	0.00154	0.00662	0.00533	29.02257	1.27172	2.13623	0.01802	479.9	27.3
Ksp 7	27.31936	0.89294	0.01251	0.00125	-0.00065	-0.00531	26.72591	1.51165	1.93642	0.02401	446.2	29.2
Ksp 8	24.54340	0.32420	0.01417	0.00168	0.00110	0.00603	24.54340	1.29329	1.87048	0.02402	413.7	26.3
Ksp 9	24.75848	0.26654	0.01225	0.00263	0.00394	0.00625	24.75848	1.16250	1.56266	0.01603	416.9	24.9
Ksp 10	25.88936	0.31186	0.01002	0.00293	0.04418	0.01133	25.10620	2.01251	1.06908	0.01203	422.1	35.1
Ksp 11	27.92564	0.44738	0.01446	0.00230	0.00535	0.01095	26.74435	2.06138	0.95891	0.01503	446.5	35.8
Ksp 12	25.86913	0.25787	0.01011	0.00166	0.00434	0.00516	25.11471	1.05162	1.89316	0.01802	422.2	23.9
Ksp 13	24.75226	0.15028	0.01484	0.00106	0.00645	0.00438	24.75226	0.80634	2.07029	0.01104	416.8	21.5
Ksp 14	24.94843	0.46151	0.01546	0.00246	0.00801	0.01348	24.34470	2.02146	0.89735	0.01603	410.7	35.2
Ksp 15	25.33357	0.32335	0.00926	0.00159	-0.00074	-0.00759	24.51474	1.56914	1.38337	0.01702	413.2	29.5
Ksp 16	25.70880	0.32955	0.01231	0.00150	0.00629	0.00538	25.13874	1.35538	1.46870	0.01802	422.6	27.1
Ksp 17	25.70167	0.20630	0.00959	0.00149	0.00585	0.00499	24.74234	0.80431	2.10485	0.01603	416.7	21.5

^{39}Ar volume = "value" x 10^{-12} cm³ STP

Note: No ^{36}Ar detectable in this sample

Reddy et al: eTable 3

Analysis	⁴⁰ Ar/ ³⁹ Ar	+-	³⁸ Ar/ ³⁹ Ar	+-	³⁷ Ar/ ³⁹ Ar	+-	³⁶ Ar/ ³⁹ Ar	+-	⁴⁰ Ar*/ ³⁹ Ar	+-	³⁹ Ar	+-	Age (Ma)	+-
Ksp 1	42.32610	1.58640	0.01679	0.00799	0.04302	0.04287	-0.00001	-0.01355	42.32925	4.30612	0.00376	0.00014	363.3	33.5
Ksp 2	43.68359	1.16114	0.01216	0.00331	-0.01399	-0.03792	0.00990	0.00522	40.75903	1.88424	0.00606	0.00016	351.0	14.8
Ksp 3	47.05227	0.93614	0.00397	0.00843	-0.04077	-0.06030	0.03584	0.01613	36.46233	4.81911	0.00265	0.00005	317.1	38.5
Ksp 4	47.38685	0.99602	0.01515	0.00228	-0.02962	-0.02721	0.02956	0.00685	38.65053	2.17604	0.00626	0.00013	334.5	17.3
Ksp 5	42.27872	0.57399	0.01764	0.00442	-0.00216	-0.01641	0.01186	0.00563	38.77356	1.74574	0.00717	0.00009	335.4	13.9
Ksp 6	47.79481	0.55217	0.01604	0.00426	-0.02355	-0.02240	0.00667	0.00392	45.82480	1.27755	0.00525	0.00005	390.3	9.9
Ksp 7	43.13400	0.67224	0.01022	0.00439	-0.00965	-0.01751	0.00970	0.00588	40.26628	1.84807	0.00721	0.00011	347.2	14.6
Ksp 8	47.30113	0.90963	0.01357	0.00412	-0.00713	-0.02064	0.00921	0.01073	44.58097	3.28649	0.00543	0.00010	380.7	25.4
Ksp 9	47.91978	1.54875	0.00928	0.00182	0.03351	0.01267	0.01761	0.01027	42.71526	3.33187	0.00624	0.00020	366.3	25.9
Ksp 10	46.35830	0.93336	0.01493	0.00391	0.06743	0.01811	0.00093	0.00762	46.08405	2.43490	0.00529	0.00010	392.2	18.7
Ksp 11	42.98689	0.71782	0.00966	0.00410	0.00712	0.02308	0.00367	0.00756	41.90386	2.34097	0.00545	0.00009	360.0	18.3
Ksp 12	48.21874	1.18430	0.01291	0.00393	0.03127	0.01988	-0.00001	-0.00391	48.22103	1.65536	0.00571	0.00014	408.5	12.7
Ksp 13	46.62025	0.96477	0.01080	0.00725	-0.01859	-0.02225	0.00086	0.01162	46.36649	3.56451	0.00585	0.00012	394.4	27.3
Ksp 14	42.95885	0.94648	0.01411	0.00838	-0.02864	-0.02892	0.00252	0.01139	42.21464	3.49089	0.00597	0.00013	362.4	27.2
Ksp 15	48.15578	0.96085	0.00727	0.00515	-0.04296	-0.02725	0.01036	0.00898	45.09387	2.80571	0.00435	0.00008	384.7	21.6
Ksp 16	47.33868	0.69108	0.01220	0.00235	-0.04638	-0.02130	0.01077	0.00646	44.15686	2.01811	0.00604	0.00008	377.4	15.7
Ksp 17	45.07028	1.24681	0.00732	0.00777	0.01362	0.03979	-0.01390	-0.01871	49.17783	5.68774	0.00288	0.00007	415.8	43.0
Ksp 18	45.14194	1.08764	0.01582	0.00481	-0.03533	-0.03009	0.00430	0.00960	43.87126	3.02656	0.00466	0.00011	375.2	23.4
Ksp 19	45.92361	1.54432	0.01671	0.00888	0.01556	0.07933	0.02379	0.01432	38.89435	4.43070	0.00252	0.00008	336.4	35.0
Ksp 20	46.99439	1.31719	0.01335	0.00474	0.05802	0.04229	0.00632	0.00944	45.12675	3.06460	0.00474	0.00013	384.9	23.6
Ksp 21	48.56009	1.09615	0.01368	0.00372	0.01166	0.02924	0.01391	0.00565	44.44874	1.94716	0.00539	0.00012	379.7	15.1
Ksp 22	47.01955	1.00769	0.01912	0.00682	0.04995	0.04186	0.01701	0.00691	41.99369	2.23301	0.00441	0.00009	360.7	17.5
Ksp 23	52.07241	1.45105	0.01314	0.00559	0.01374	0.04246	0.00998	0.01498	49.12356	4.63243	0.00401	0.00011	415.3	35.0
Ksp 24	44.96257	0.71749	0.01645	0.00350	-0.01597	-0.01250	0.02030	0.00781	38.96355	2.39033	0.00640	0.00010	336.9	18.9
Ksp 25	47.99843	0.81004	0.01578	0.00413	-0.01573	-0.02826	0.01099	0.00640	44.75075	2.03724	0.00501	0.00008	382.0	15.8
Ksp 26	50.00543	0.96337	0.01335	0.00668	0.05495	0.03484	0.00104	0.01102	49.69748	3.39502	0.00474	0.00009	419.7	25.6
Ksp 27	46.45627	1.21979	0.01273	0.00547	-0.00408	-0.02642	0.01812	0.01068	41.10134	3.33479	0.00579	0.00015	353.7	26.1
Ksp 28	43.34380	1.08320	0.02177	0.00656	0.01959	0.02422	-0.01034	-0.01491	46.39882	4.55375	0.00484	0.00012	394.6	34.8
Ksp 29	40.68492	0.77598	0.01921	0.00289	0.03203	0.03375	-0.00406	-0.00860	41.88466	2.66220	0.00494	0.00009	359.8	20.8
Ksp 30	54.93809	1.21408	0.01141	0.00606	0.00428	0.04755	0.00271	0.01579	54.13841	4.81582	0.00369	0.00008	452.8	35.7

³⁹Ar volume = "value" x 10⁻¹⁰ cm³ STP